EuCARD-2

Journal Publication

Conceptual design of a non scaling fixed field alternating gradient accelerator for protons and carbon ions for charged particle therapy

Peach, K. J. (John Adams Institute) *et al*

11 March 2013

Conceptual design of a nonscaling fixed field alternating gradient accelerator for protons and carbon ions for charged particle therapy

K. J. Peach,[1,*] M. Aslaninejad,[2] R. J. Barlow,[3] C. D. Beard,[4,†] N. Bliss,[4] J. H. Cobb,[1] M. J. Easton,[2] T. R. Edgecock,[5,3] R. Fenning,[6] I. S. K. Gardner,[5] M. A. Hill,[7] H. L. Owen,[8,9] C. J. Johnstone,[10] B. Jones,[7] T. Jones,[4] D. J. Kelliher,[5] A. Khan,[6] S. Machida,[5] P. A. McIntosh,[4,9] S. Pattalwar,[4] J. Pasternak,[2,5] J. Pozimski,[2,5] C. R. Prior,[5] J. Rochford,[5] C. T. Rogers,[5] R. Seviour,[3] S. L. Sheehy,[1,‡] S. L. Smith,[4] J. Strachan,[4] S. Tygier,[8,9] B. Vojnovic,[7] P. Wilson,[7,§] H. Witte,[1,∥] and T. Yokoi[1]

[1]*John Adams Institute for Accelerator Science, Department of Physics, University of Oxford, Oxford OX1 3RH, United Kingdom*
[2]*Department of Physics, Imperial College, London SW7 2BZ, United Kingdom*
[3]*School of Applied Sciences, University of Huddersfield, Queensgate, Huddersfield HD1 3DH, United Kingdom*
[4]*STFC Daresbury Laboratory, Warrington, Cheshire WA4 4AD, United Kingdom*
[5]*STFC Rutherford Appleton Laboratory, Chilton, Oxfordshire OX11 0QX, United Kingdom*
[6]*Brunel University, Uxbridge, Middlesex UB8 3PH, United Kingdom*
[7]*Gray Institute for Radiation, Oncology and Biology, Department of Oncology, University of Oxford, Oxford OX3 7DQ, United Kingdom*
[8]*Manchester University, Manchester M13 9PL, United Kingdom*
[9]*Cockcroft Institute, Daresbury Laboratory, Keckwick Lane, Daresbury, Warrington, Cheshire WA4 4AD, United Kingdom*
[10]*Fermi National Accelerator Laboratory, P.O. Box 500, Batavia, Illinois 60510, USA*

The conceptual design for a nonscaling fixed field alternating gradient accelerator suitable for charged particle therapy (the use of protons and other light ions to treat some forms of cancer) is described.

I. INTRODUCTION

The conceptual design is presented for a particle accelerator for medical applications (PAMELA), an accelerator facility to deliver protons and carbon ions efficiently for charged particle therapy (CPT). The design uses the novel features of nonscaling fixed field alternating gradient (ns-FFAG) technology to improve performance over existing facilities. The fixed field allows more rapid acceleration than is possible with a synchrotron (kHz rather than Hz) while still allowing variable energy extraction from 70 to 250 MeV for protons, and 110 to 440 MeV/u for carbon, with excellent dose control and fast transverse scanning. This should result in greater patient throughput owing to shorter treatment durations and perhaps fewer treatment sessions (fractions), and eventually lower cost.

Current technology [1,2] uses cyclotrons or synchrotrons to accelerate the ions. Cyclotrons are relatively simple machines with some flexibility and high current capability. With the exception of H⁻, they are essentially fixed energy extraction, and require degraders to modulate the energy and these inevitably degrade the beam characteristics, reduce intensity, and induce radiation to the environment around the degrader especially in the case of carbon ions. Synchrotrons with the slow extraction mode have variable energy but the rate at which the energy can be varied is limited and relatively slow leading to longer treatment times. In addition, it requires large intensity stored beams (with space charge limitations) to allow for the fast transverse scanning. Rapid cycling synchrotrons have been proposed with a frequency up to 50–60 Hz but may be limited by the magnet ramping rate [2]. Spot scanning techniques impose even more stringent demands on the accelerator systems. While the present generation of proton and carbon ion facilities are certainly capable of delivering therapeutically useful beams, it would be even better if the limitations discussed above were removed; more rapid energy changes in principle allow finer layer scanning and more repainting with the potential for improved optimization of the treatment planning. This means, in effect, trying to find a technology that has the flexibility to deliver variable energy beams typical of a synchrotron with the high current capability of the cyclotron, and the ability to vary the energy at high rates. The fixed field alternating gradient (FFAG) accelerator [3–5] would seem to satisfy both of these requirements. In addition, like the synchrotron, FFAGs should avoid the radiation load on an energy selector (degrader). The original 1960s FFAG
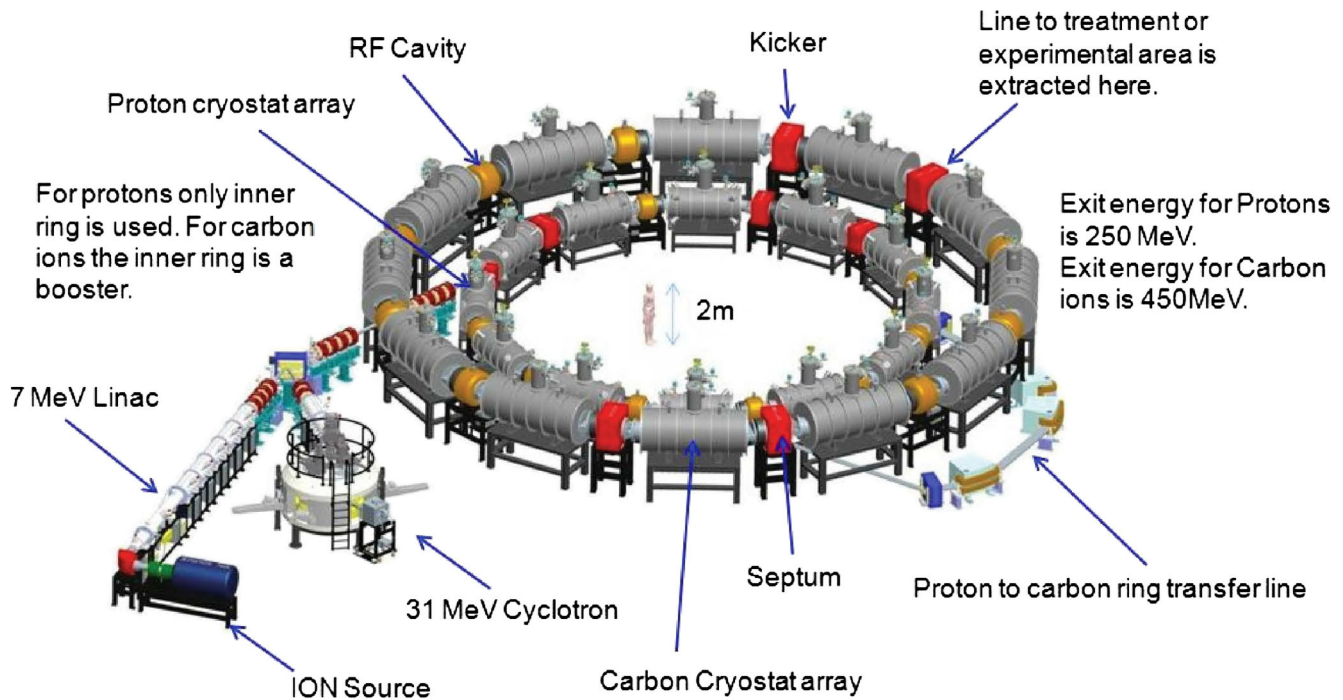

FIG. 1.   Proposed PAMELA layout.

designs (now called *scaling FFAG* accelerators) required very large magnets with complex field shapes and large orbit excursions. In the late 1990s [6], it was realized that if the scaling requirement was relaxed (essentially that the horizontal and vertical tunes remained constant through acceleration), the magnets became much simpler (combined function dipole and quadrupole), easing considerably the construction. However, the variable tunes meant that resonance crossing had to be addressed; simulation indicated that, provided that the acceleration was sufficiently fast, the beam could be accelerated. This is the nonscaling FFAG accelerator, now being tested with the electron model for many applications (EMMA) [7], and recently shown to work [8].

Originally, it was thought that a dense EMMA-like lattice might be suitable for a proton and carbon ion therapy machine. However, detailed studies [9–11] showed that such lattices are very sensitive to alignment and field errors, and the dense lattice meant that it was difficult to accommodate the relatively large variable frequency rf cavities needed for acceleration. It was also difficult to generate rapid enough acceleration to render the resonances benign, and the injection and extraction angles were unreasonably large. An alternative approach was adopted following the design methodology described in [12]. Essentially, starting with a scaling FFAG, the scaling conditions are gradually violated while, at each step, approximate scaling is restored by adjusting the lattice parameters. The result is a *nonlinear* nonscaling FFAG accelerator with the required performance (fast accelera-

tion, rapid cycling, variable energy, high current). The layout of PAMELA is shown in Fig. 1.

The clinical requirements and the desirable features governing the mode of operation are discussed briefly in the next section, since these determine the main performance requirements of the accelerator. The following sections discuss the main acceleration system, main ring magnets, rf and the injection and extraction scheme, followed by discussion of the ion sources, beam transport to the treatment rooms, and the gantry design.

II. CLINICAL REQUIREMENTS

About half of cancer patients will receive radiation therapy during treatment, mostly x rays from an electron linear accelerator. There has been rapid development, particularly over the past 20 years, of increasingly sophisticated treatment planning algorithms to target the dose more effectively on the tumor while sparing as far as possible healthy tissues and vital organs. Charged particle therapy is even more challenging because the finite range of the ions places strict demands upon the accelerator complex. These demands are discussed below from a clinical perspective [see for example [13]].

In radiation therapy, the ability to form the best possible dose distribution in accordance with treatment planning requirements is of paramount importance. The advantage of particle therapy over conventional x-ray based radiation therapy is the dose selectivity due to the Bragg peak. This can minimize unnecessary dose in normal tissues proximal

to the target volume and allows tissue beyond the target volume to be almost or entirely dose-free. These features are ideal for radiation therapy. On the other hand, to obtain such an advantage, particle therapy requires more delicate dose control and more precise imaging information concerning the internal structure of the patient and tumor position.

Until relatively recently, most patients were treated with a broad beam scheme, formed by either double scattering or wobbling the beam [1]. With the broad beam, a collimator trims the horizontal dose field to fit the lateral shape of the tumor, while in the longitudinal direction conformity of the dose field is achieved using a "bolus," which is a machined energy degrader to adjust particle local range to fit the distal target shape, and the tumor is irradiated in depth by varying the energy [the so-called "spread out Bragg peak" (SOBP)]. The most serious clinical problem in the broad beam irradiation is that the conformity is well matched only at the distal edge, since the bolus adjusts only the range while the width of the SOBP is constant over the entire target volume. Consequently, there is an inevitable high dose region in healthy tissue on the proximal side. In addition, the quality of the beam is inevitably degraded, and there is also a small flux of neutrons.

To overcome the drawbacks of the conventional broad beam irradiation, "active scanning irradiation" was proposed [14]. In this scheme, a target volume is subdivided into small volumes, the so-called "voxels," which are individually irradiated with a scanned pencil beam. The scheme in principle provides excellent dose conformity over the entire target volume, and markedly reduces the unnecessary dose in healthy tissue on the proximal side. Furthermore, by varying the locally deposited dose given by the pencil beam at each voxel, it can also achieve more flexible dose distributions to maximize therapeutic gain.

As the irradiation scheme is fully active, the passive elements such as collimators, bolus, and scattering foils can be eliminated from the treatment, and the intensity loss due to these devices is no longer a problem; there may also be a reduction in the secondary neutron dose. These features are expected to improve the treatment efficiency considerably. Because of the clinical and practical flexibility and efficiency, active scanning is considered as a key technology for the next generation of particle therapy, and newly planned or recently built facilities are all equipped with active scanning.

A summary of the clinical requirements for PAMELA is given in Table I.

III. OVERVIEW

The conceptual design for a combined proton and carbon ion therapy machine is presented using a nonscaling fixed field alternating gradient accelerator. The machine is capable of delivering high dose rates in spot scanning mode, with kHz variable energy extraction. The design is a "proof of principle" that such a machine can meet the demanding clinical requirements. The design includes not only the central accelerators but also preliminary ideas for the ion sources, injection and extraction, beam transport, and gantries, which require novel solutions if the rapid energy variation capabilities of the FFAG are to be fully utilized.

The principal features of the design are summarized below, with some ideas for further optimization.

(i) The proton source is taken as a commercial 31 MeV cyclotron, with a custom design ion source capable of delivering C^{6+} carbon ions at a matched energy. In a future development, it would be interesting to look at extending the C^{6+} ion source also to accelerate H_2^+, which would allow in principle other light ions (especially $^4_2$He or $^6_3$Li) to be used.

(ii) The main accelerator has two rings—the first ring accelerates protons to the full energy required for therapy (250 MeV) and C^{6+} to 68.8 MeV/u, with a second ring to accelerate the C^{6+} to the full energy.

(iii) The injection scheme has been designed and shown to be feasible, with a single kicker and septum. The extraction scheme is more challenging because of the need to extract at variable energy, which means at variable lateral position, requiring a kicker and a novel septum with horizontal field gradient. For practical reasons, vertical extraction is preferred.

(iv) Preliminary ideas for a beam transport are presented, capable of transporting the beam from the accelerator to the treatment rooms (whether fixed beam or gantry) across the whole energy range using a fixed field (FFAG-like) arrangement.

(v) Preliminary ideas are presented for an FFAG gantry which can transport the beam across the whole energy range, with minimal dispersion at the patient. Ideas are

TABLE I. Summary of clinical requirement of PAMELA.

Parameter	Value	Unit
Horizontal dose field size	15×15	cm
Maximum SOBP width	10	cm
Maximum depth	25	cm
Maximum depth variation	13	cm
Energy range (p)	70 to 250 (300)[a]	MeV
Energy range (C)	110 to 440	MeV/u
Dose field uniformity	<2	%
Dose field tolerance	<2	%
Beam spot size (FWHM)	4×4 to 10×10	mm
Scanning rate	>100	Voxel/sec
Scanning speed	0.5 (<1)	cm/m sec
Energy step	0.5 to 2	MeV
Single dose	1 to 7	Gy
Intensity range	0.05 to 1.5	nA
Bunch intensity	2.5×10^5 to 6.5×10^6	ppp

[a]For proton radiography.

presented for achieving the lateral beam sweeping for spot scanning. The main issue to be resolved is the gantry size.

The PAMELA design presented here is the result of detailed simulations of the principal components, from the (carbon) ion source to the gantry.

IV. LATTICE DESIGN

In order to provide both protons and fully stripped carbon ions for particle therapy, the PAMELA design envisages a concentric or near-concentric two-ring solution, both based on a novel concept in FFAG lattice design [12]. The lattice is presented together with the performance of both rings of the full proton and carbon facility. The energies and corresponding magnetic rigidities required in each ring are given in Table II.

A. General considerations

When it was invented more than 50 years ago, the optics of the FFAG was designed to keep the transverse betatron tunes constant throughout acceleration [4,5]. The magnetic field profile was chosen in the form

$$B_y(r, \theta) = B_0(r/r_0)^k F(\theta), \quad (1)$$

where r and y are radial and vertical coordinates, respectively, the suffix 0 denotes the reference value, the field index is given by k, and $F(\theta)$ is a periodic function around the ring representing the symmetry of the lattice cell structure. A local Cartesian coordinate frame will also be used, in which the x coordinate is horizontal [equivalent to r in Eq. (1)], y is vertical and z is perpendicular to x and y and follows the particle direction (equivalent to s in optical tracking codes such as MAD-X [15]). A key feature of this type of FFAG is that while the closed orbits depend on particle momentum, the focusing remains constant and all the orbits are enlargements of each other. This type of machine is called a scaling FFAG and both the radial and sector type machines have been built. In a scaling FFAG, the orbit excursion throughout acceleration is typically on the order of 1 m, governed by the field index k which determines the focusing strength. Increasing the field index to reduce the orbit excursion can result in unstable optics,

owing to the change in phase advance. A large orbit excursion is therefore typical in scaling FFAGs and makes the magnets larger than those of a conventional synchrotron, though still much smaller than the magnets of a cyclotron.

Recently, a new type of FFAG accelerator was proposed to decrease the orbit excursion and simplify the magnetic field profile [16–18]. The lattice is made from only dipole and quadrupole magnets, which have a linear field instead of the more complicated field profile of the scaling FFAG. The orbit excursion is minimized to the order of millimeters while maintaining the phase advance in a reasonable range. The price paid for these advantages is that the transverse tune is no longer constant and the beam goes through many resonances at integer and half-integer tunes in the process of acceleration. This is called a linear nonscaling FFAG.

Beam deterioration due to resonance crossing depends on the strength of the resonance and the crossing speed [19]. Resonance phenomena are likely to become more troublesome if the crossing is done over a sufficiently long time scale. This type of linear nonscaling FFAG was originally proposed for muon acceleration where the acceleration is completed within 10 to 20 turns and where the machine tune changes by one unit per turn. In this time scale, it is now known that there is no accumulation of orbit distortion due to resonances. Instead, a particle is kicked incoherently when an error field exists in a lattice [20].

When the linear nonscaling FFAG is applied to a slower cycling machine as would be the case for a particle therapy accelerator, resonance crossing can become a serious problem [9]. Although the integer and half-integer resonances are all nonstructural, the allowed tolerance of alignment and field profile becomes very small, around a few μm, which is very difficult to construct with current technology.

Several methods of keeping the transverse tune constant in a linear nonscaling FFAG were proposed to overcome the potential problems caused by resonance crossing. In conventional terminology this may be referred to as chromaticity correction. Johnstone *et al.* introduced the idea of using a wedge shaped quadrupole magnet, in which the edge focusing and path length of the quadrupole were each made a function of beam momentum [21]. It was shown that an almost flat tune over the wide momentum range of a factor of 6 is achievable without crossing major resonances.

Another strategy to avoid resonance crossing was proposed [22] in which a more conventional method of chromaticity correction is applied to a linear ns-FFAG. This involves adding a sextupole and octupole component to correct the natural chromaticity, where the strength of these components is determined by the downhill simplex method. Unfortunately, chromaticity correction of this type results in a machine which has complex multipole magnets and a similar orbit shift to a scaling FFAG. The

TABLE II. Particle kinetic energies and magnetic rigidities for the two-ring complex, where "inj" is the injection energy to the ring and "ext" is the highest extraction energy for each ring. Note that the second ring could accelerate protons to 1.2 GeV for radiography.

Particle	H^+		C^{6+}		
Ring 1	inj	ext	inj	ext	
Ring 2				inj	ext
Energy [MeV/u]	31 MeV	250	7.9	68.8	440
$B\rho$ [T m]	0.811	2.432	0.811	2.432	6.716

reason for this is twofold. First, chromaticity correction is usually applied where the dispersion function is largest as it is most effective at this point. However, the dispersion function in linear ns-FFAGs tends to be small as this gives the desirable property of a smaller orbit shift. This means that the nonlinear magnet strengths to obtain chromaticity correction must be large in such a machine. Second, the upper limit on cell tune variation is inversely proportional to the number of cells. The requirement that the total tune variation is restricted to within an integer (or preferably half an integer) indicates that a small number of cells is preferable, whereas a linear ns-FFAG tends to have a large number of cells. This makes chromaticity correction even more challenging.

In addition to the resonance crossing phenomena, existing concepts for linear nonscaling FFAGs for proton therapy had the general feature of being very densely packed with magnets, allowing only short straight sections for injection, extraction, and rf cavities, usually less than 0.5 m. This is a particular concern for fully stripped carbon ions, where the higher magnetic rigidity means that long straight sections become crucial, particularly for extraction.

To overcome the resonance crossing issues and provide longer straight sections of over 1 m, a new lattice design approach has been adopted. This design begins with a scaling FFAG and makes a number of changes that break the scaling law, while retaining the small tune variation which is required. Additional positive features emerge from this design such as a reduced orbit excursion and simplified magnets. In fact, it was found that the orbit excursion of a scaling FFAG could be significantly reduced if the FDF triplet focusing structure was adopted and a large field index in the second stability region of the solution of Hill's equation was used, where F is a focusing and D is a defocusing magnet [23]. Although the orbit excursion cannot be of the order of millimeters like that in a linear nonscaling FFAG, a reduction of about a factor of 5 from a scaling FFAG is expected. Note that the reference orbits do not pass through the magnetic centers and so the FDF triplet provides focusing in both planes and bending in the horizontal plane.

B. Proton ring design

Starting with the concept of a radial-sector FDF triplet scaling FFAG, a number of changes and simplifications are made [12].

First, the magnetic field no longer follows the scaling field profile, so the design becomes nonscaling. The scaling field profile is expanded and only the dipole and first few multipoles are retained. This significantly changes the magnet design, allowing superconducting magnets to be employed rather than iron-cored magnets with complicated pole shaping used in a scaling FFAG. To ease cost, construction, and alignment issues, the magnets are made

rectangular rather than sector shaped and are aligned along a straight line in each cell rather than along an arc, further violating the scaling law.

A number of parameters can be used to characterize the PAMELA lattice design, including the field index k and geometrical factors including the lattice packing factor, magnet length, and average radius. The field index k influences both the magnetic focusing strength and the orbit excursion, that is, the difference in radial position of the maximum and minimum energy orbits, as shown by the two dotted lines in Fig. 2. A large field index results in a small orbit excursion, which is advantageous as it reduces the bore of the magnets, the beam pipe aperture, and the rf aperture. However, the field index is limited when using the first stable region of Hill's equation, where the phase advance per cell is less than 180°.

In this design the second stable region of the solution to Hill's equation is used, with a horizontal phase advance per cell greater than 180°. This allows for a larger field index to be used, resulting in a smaller orbit excursion. The available working points as a function of field index and D/F magnet strength ratio are shown in Fig. 3.

By carefully choosing the field index to be large, here $k = 38$, a D/F ratio is then selected which results in cell tunes of around $\nu_x = 0.72$, $\nu_y = 0.27$ which are later optimized. In this case the maximum field values are 4.0 T in the D magnet and 4.25 T in the F.

The lattice packing factor, α, is the total length of the FDF triplets compared to the machine circumference. In order to access the second stable region of Hill's equation for an FDF triplet focusing lattice while maintaining suitable dynamics, it is preferable to have a small ($\alpha \approx 0.5$) packing factor [23]. However, too small a value for α results in short magnet lengths. This may result in
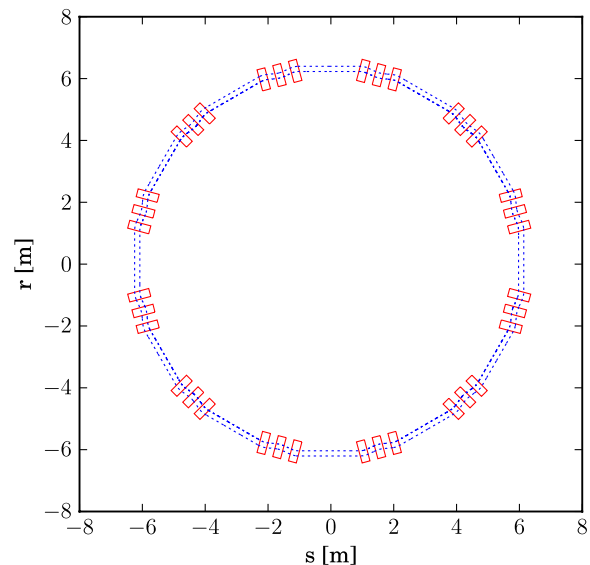

FIG. 2.   Layout of the proton lattice with injection orbit (inner dotted line) and maximum energy orbit (outer dotted line).
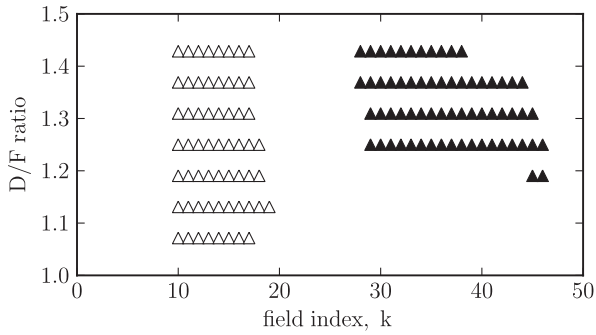
FIG. 3. Regions of stable optics for proton lattice. The second stability region of the solution of Hill's equation is shown in black filled points.

unachievable magnetic fields or, to compensate, a very large radius of the accelerator. For these reasons α is chosen to be suitably large to achieve a compact accelerator while preserving the stable dynamics, in this case $\alpha = 0.48$. Once the packing factor and average radius are chosen, the peak magnetic field can be reduced slightly by extending the magnets into the short drift space, ensuring the magnetic center remains fixed. This design strategy results in a lattice which has some important differences to both scaling FFAGs and linear nonscaling FFAGs. These differences can be summarized as follows.

(1) The scaling law is approximated as a Taylor series (and later a polynomial fit) and truncated at the octupole or decapole, breaking the scaling law and making the machine nonscaling.

(2) The magnets, rather than being sector shaped as in a scaling FFAG, are made rectangular, in order to reduce costs in manufacturing.

(3) The magnets in each triplet cell are aligned along a straight line, rather than along the arc of a circle described at the machine radius, which should ease alignment and the production of other systems, such as cryogenics, which will need to be integrated (see Sec. V).

TABLE III. Parameters for the proton and carbon ring lattices.

Parameter	Unit	Value
Proton ring number of cells		12
Proton ring reference radius r_0	m	6.251
Proton ring magnet length	m	0.3144
Proton ring packing factor α		0.48
Proton ring field index, k		38
Proton ring orbit excursion	m	0.176
Carbon ring number of cells		12
Carbon ring reference radius r_0	m	9.3
Carbon ring magnet length	m	0.6330
Carbon ring packing factor α		0.65
Carbon ring field index, k		42
Carbon ring orbit excursion	m	0.217

(4) The second stable region of Hill's equation is used, with a horizontal phase advance per cell greater than 180°, allowing a larger field index to be used, resulting in a factor of 5 reduction in orbit excursion.

(5) Depending on the ratio of cell length to machine circumference, the straight sections between cells can be increased to provide a long straight section of over 1 m, while preserving stable dynamics.

The idealized layout of the lattice design is shown in Fig. 2 and the baseline parameters of the PAMELA proton lattice are given in Table III.

Simulation software used for the PAMELA lattice design include the ray-tracing code ZGOUBI [24] for tracking studies and S-CODE [25] for the variation of basic lattice parameters.

1. Beta functions and tune variation

The beta functions in one cell, as calculated with S-CODE, are shown in Fig. 4.

As mentioned above, the scaling field profile is expanded about some expansion radius r_0 and multipole terms from dipole to decapole are included. This expansion to the fourth order can be written as in Eq. (2):

$$
B_y = B_0 \left[1 + \frac{k(r - r_0)}{1! r_0} + \frac{(k-1)k(r - r_0)^2}{2! r_0^2} \right.
$$
$$
+ \frac{(k-2)(k-1)k(r - r_0)^3}{3! r_0^3}
$$
$$
\left. + \frac{(k-3)(k-2)(k-1)k(r - r_0)^4}{4! r_0^4} \right]. \quad (2)
$$

The departure of the magnetic field from the ideal field profile depends on both the distance from the expansion radius and on the number of multipole terms added. In order to minimize the distance over the momentum range, the expansion radius should be set to the center of the orbit excursion. The orbit excursion can be established, *a priori*, by finding the maximum and minimum momentum trajectories in the scaling FFAG case. The appropriate r_0 and
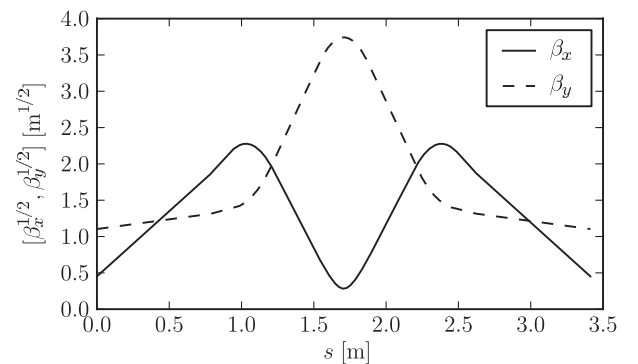

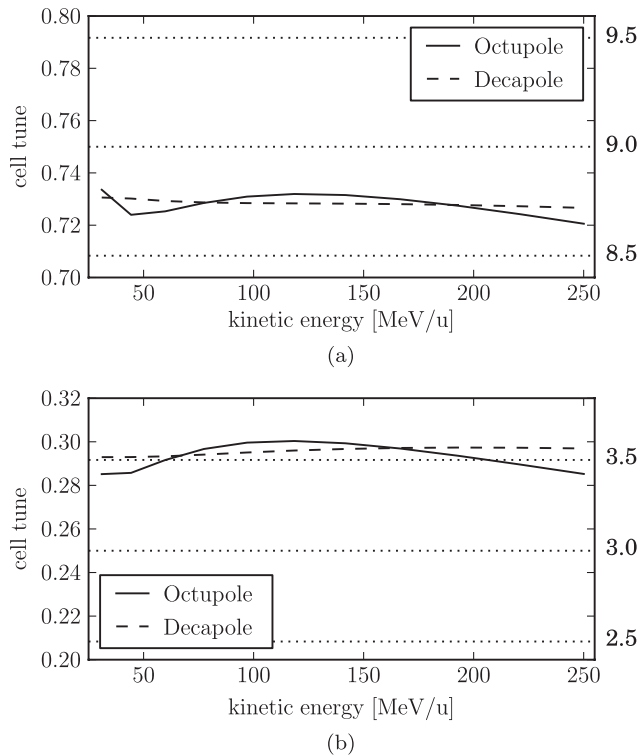FIG. 4. Beta functions in one cell of proton lattice.

(a)

(b)

FIG. 5.   Cell tunes for the proton ring throughout acceleration for the case of rectangular shaped magnets using a polynomial fit to the ideal field profile. The three magnets are aligned parallel with each other. Horizontal cell tune in (a) and vertical cell tune in (b). Dashed lines and associated numbers show total tune of a 12 cell ring.

corresponding field B_0 to use in the expansion equation is then established.

Second, the number of necessary multipole components that give an acceptable tune variation over the momentum range can be determined. The tune variation (as calculated by ZGOUBI) when multipoles up to the octupole and decapole are included is shown in Fig. 5 and the tune variations are given in Table IV. The variation of the total machine tune in both the octupole and decapole case are well within half an integer. These results illustrate that the design method for constraining betatron tunes is successful.

2. Tracking results and dynamic aperture

A typical tracking example using ZGOUBI including acceleration is shown in Fig. 6, clearly showing the small

TABLE IV.   Variation of cell ($\nu_{x,y}$) and total ($Q_{x,y}$) tunes as a result of changing the order of polynomial fit for rectangular shaped magnets aligned parallel to each other.

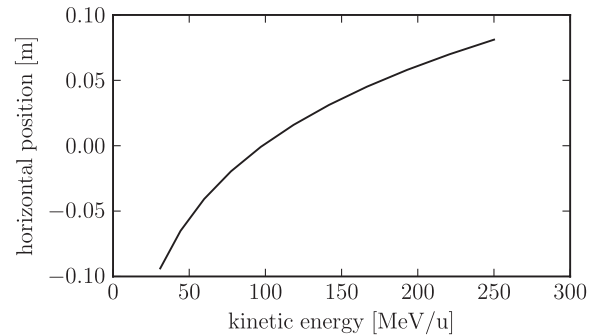| Multipole order	ν_x	ν_y	Q_x	Q_y
Octupole	0.0130	0.0152	0.1560	0.1824
Decapole	0.0040	0.0044	0.0476	0.0528

FIG. 6.   Change in closed orbit position through acceleration, tracked using ZGOUBI.

natural orbit excursion, which at its largest value is 0.18 m at the center of the D magnet.

This lattice was designed to overcome the high sensitivity of densely packed nonscaling FFAG lattices to alignment errors. To ascertain the sensitivity of the current lattice design to alignment errors, Gaussian distributed patterns of random horizontal alignment errors were introduced to each magnet in the lattice, using ten different values of the standard deviation σ from 0 to 100 μm in steps of 10 μm. The Gaussian distributions are cut off at 3σ, which removes very large errors which could have a dominant effect on the dynamics. For each value of σ, a different random value is applied to each of the lattice magnets and a single particle is tracked to extraction over 1000 turns. Synchrotron motion is neglected as only the transverse dynamics are of interest here and the "cavities" are represented as zero-length elements providing a simple energy gain. Other effects such as synchrobetatron resonances should be studied as part of the next phase. The orbit distortion is calculated as the maximum difference between the distorted particle orbit and the orbit of a particle in an error-free lattice. This is repeated 10 times for each σ value and the mean and rms values of the orbit distortion are calculated.

Distortion is quantified in terms of the "amplification factor," A, as in Eq. (3):

$$A = \frac{\langle \text{orbit distortion [mm]} \rangle}{\langle 1\sigma \text{alignment error [mm]} \rangle}. \tag{3}$$

The amplification factors are obtained by fitting straight lines to the mean of the distributions shown in Fig. 7 and the error on the amplification factor corresponds to the difference between the maximum/minimum linear fit and the central fit. The errors are relatively large as the main contribution to the distortion is the difference between the closed orbits of the error-free lattice and the misaligned lattice, rather than the distortion of the single particle orbit.

The amplification factor with acceleration is 5.81 $\pm$ 3.95 (horizontal) and 9.47 $\pm$ 5.13 (vertical). The alignment tolerances in this machine are considerably more relaxed than in the case of a linear ns-FFAG design. These results indicate that, for an allowed orbit distortion of $\approx$ 1 mm,
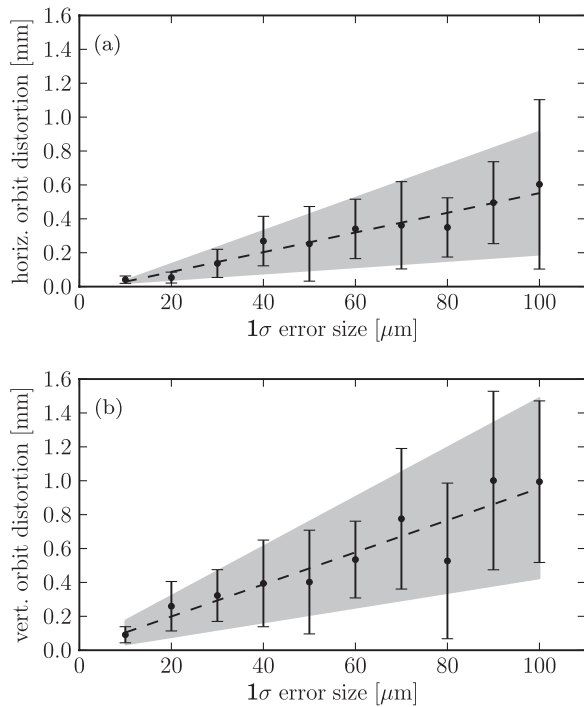
FIG. 7. Orbit distortion as a result of introducing horizontal and vertical alignment errors to the proton ring. The black points correspond to the mean of the ten runs at each σ value and error bars correspond to the rms spread of the ten runs. The shaded region is the area between the maximum and minimum linear fit, where the central linear fit determines the amplification factor in each case. (a) Fitted distribution of horizontal alignment errors. (b) Fitted distribution of vertical alignment errors.

the alignment tolerances must be better than around 100 μm. This tolerance level has been routinely achieved in other accelerators.

The dynamic aperture was calculated for rectangular magnets with parallel alignment. The calculation covers a cell tune range of 0.7–0.75 and 0.25–0.30 in the horizontal plane and vertical plane, respectively. In each scan, the tune in just one transverse plane is varied while in the other transverse plane it is fixed at the nominal value. The calculation is made at injection energy to study the case where the beam is at its largest size in physical space. An error-free lattice is assumed and multipole components up to decapole from a polynomial fit to ideal field strength are included. To select a particular value in the tune space, the field index k (and hence the coefficients of each multipole term) and the ratio of the F and D strength are adjusted.

The search for dynamic aperture begins by tracking a single particle over 1000 turns. The particle has identical starting conditions in both planes. In each case the initial coordinate is given by $-\sqrt{2\mathbf{J}/\gamma_{x,y}}$ and the initial angle is zero; $\mathbf{J}$ is the action variable and $\gamma_{x,y}$ is the horizontal or vertical Twiss parameter. The tracking is started at $2\mathbf{J} = 1\pi$ mm mrad normalized amplitude and then increased in
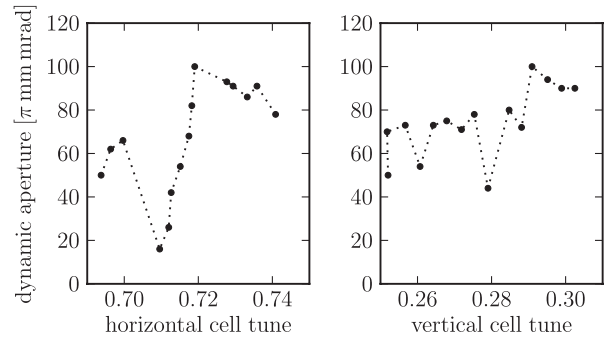

FIG. 8. Dynamic aperture vs (left) horizontal cell tune (ν_x), (right) vertical cell tune (ν_y). The optimized lattice of rectangular shaped magnets with polynomial fit to strength is used.

steps of 1π mm mrad until the particle is lost. The dynamic aperture is given by the highest amplitude particle that survives tracking.

It is clear from the results shown in Fig. 8 that it is possible to choose a point in the tune space where the dynamic aperture is more than 50π mm mrad normalized in both transverse planes, which is sufficient for the application of CPT. One of the local minima in the dynamic aperture results can be attributed to a coupling between the transverse planes. Since there is no skew quadrupole component present a resonance at $\nu_x + \nu_y = 1$ is discounted. Instead the observed coupling is attributed to the octupole term driving a fourth order resonance at $2\nu_x + 2\nu_y = 2$.

C. Carbon ring design

Ideally the lattice for the carbon ring should follow the same concept as the smaller proton lattice, but poses an even greater challenge as the charge-to-mass ratio of C^{6+} is only half that of protons. This leads to a higher required energy and higher magnetic rigidity of the particles. The highest rigidity reached by C^{6+} ions at 440 MeV/u is 6.716 T m; more than double the 2.432 T m of full energy protons. Nonetheless, the ring radius should be much less than double the radius of the proton machine, while maintaining long straight sections for injection/extraction and realistic magnet designs.

The following requirements are imposed on the design of the carbon lattice.

(1) Long straight sections of greater than 1.2 m are required in order to fit the rf system, injection and extraction sections.

(2) The total magnetic bore diameter needs to be less than 0.35 m. This is to minimize the ratio of magnet bore to length, where a practical magnet length should be less than about 1 m.

(3) The peak magnetic field must be less than 4.5 T to ensure that realistic superconducting magnets can be designed. This is in line with experience from designing the proton lattice.
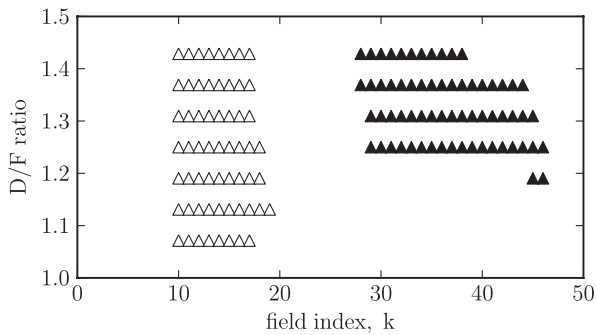
FIG. 9. Stable working points for the 9.3 m carbon lattice design with a packing factor of 0.65. The second stable region is shown in black filled points.

(4) Total tune variation should be less than half an integer in both planes in order to avoid resonance crossing.

(5) The radius of the carbon ring needs to be at least 1.5 m greater than the proton ring to allow the possibility of concentric rings.

The process of selection of the baseline parameters for the PAMELA carbon lattice necessarily involved consultation with magnet and rf designers. Initial discussions were based on an 8.5 m radius lattice; however, high peak fields observed in a preliminary magnet design necessitated an increase in radius. After a number of iterations a 9.3 m radius was selected to lower the peak current on the superconducting wires in the magnet design. A consequence of this is that, given the limitations on the achievable magnetic field, the packing fraction α is 0.65 (see Table III); this is a larger packing factor than desirable, but this "soft" requirement was over-ridden in favor of compactness—a packing factor of 0.65 retains good dynamics and reasonable access to the second stability region as shown in Fig. 9.

The design procedure used for the proton ring is carried out for the 9.3 m radius carbon lattice design, as this was deemed the most likely feasible solution. For this configuration, the lattice parameters are outlined in Table III and the stable working points are shown in Fig. 9.
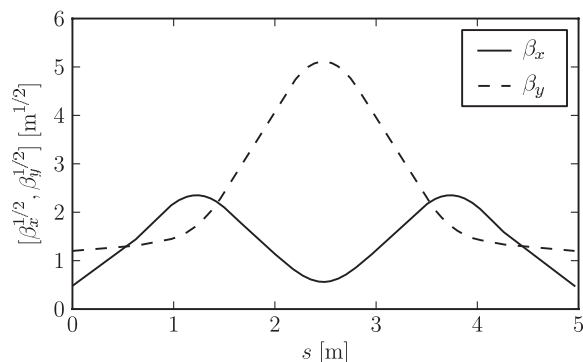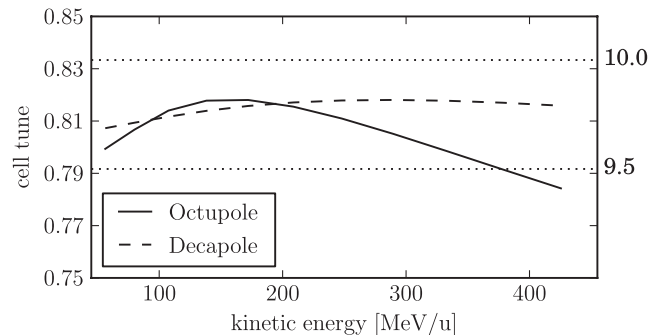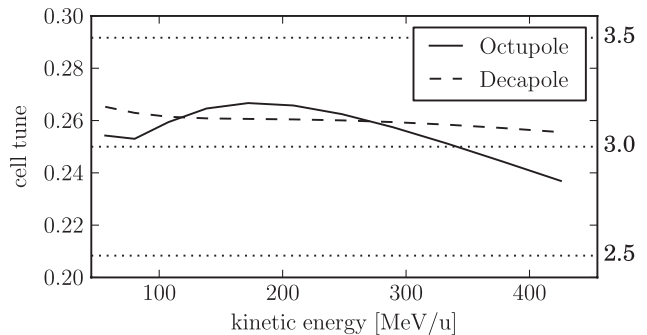

FIG. 10. Beta functions in one cell of the carbon lattice as calculated with S-CODE.

(a)

(b)

FIG. 11. Variation of horizontal cell tune (a) and vertical cell tune (b) for different orders of multipoles for the carbon ring. Dotted lines correspond to integer and half-integer resonances of the total machine tune.

1. Beta functions and tune variation

The beta functions at the reference momentum in one cell of the carbon lattice as calculated with S-CODE are shown in Fig. 10.

The variation of betatron cell tunes throughout acceleration is shown in Fig. 11 for polynomial fits to the ideal field law corresponding to magnetic multipoles up to octupole and decapole. The total machine tune variation for each case is given in Table V. In both cases the tune variation is less than half an integer. The operating point can be shifted to avoid the half-integer resonance currently crossed at high momentum in the octupole case.

2. Tracking results and dynamic aperture

The total orbit excursion throughout acceleration is shown in Fig. 12. The total change in orbit position between the lowest energy (110 MeV/u) and highest energy

TABLE V. Variation of cell ($\nu_{x,y}$) and total ($Q_{x,y}$) tune for different orders of polynomial fit to the ideal field profile.

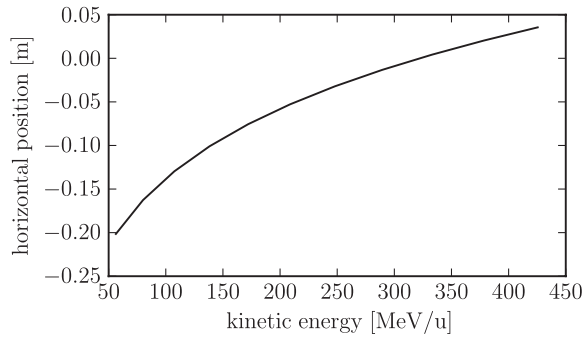| Multipole order	ν_x	ν_y	Q_x	Q_y
Octupole	0.0338	0.0298	0.4056	0.3574
Decapole	0.0108	0.0097	0.1297	0.1165

FIG. 12.　Variation of orbit position in the horizontal direction during acceleration.

(440 MeV/u) orbits is about 24 cm for the energy range required.

The dynamic aperture is calculated using the same method as for the proton ring, at the injection energy (68.8 MeV/u) for a range of horizontal and vertical tunes, determined by changing the k value and ratio between the F and D strengths. The optimized carbon lattice using a polynomial fit up to decapole is assumed with no alignment errors present. Single particles are tracked over 1000 turns, starting with the same normalized amplitude in both horizontal and vertical planes. The amplitude is then increased until the particle is lost, and the dynamic aperture plotted next to each point in Fig. 13 is the highest amplitude surviving particle in units of π mm mrad normalized. In this case the dynamic aperture is greater than 50π mm mrad for most tune values, which is sufficient for this application, except where the vertical tune is close to 0.25; as noted above, the machine tune can in principle be moved to avoid this resonance.

D. Proton to carbon ring transfer line

A transfer line is required to take carbon ions at 68.8 MeV/u from the proton ring and deliver them through an optically matched line into the carbon ring. As injection and extraction from both rings is vertical, the transfer line must cancel both vertical and horizontal dispersion. The
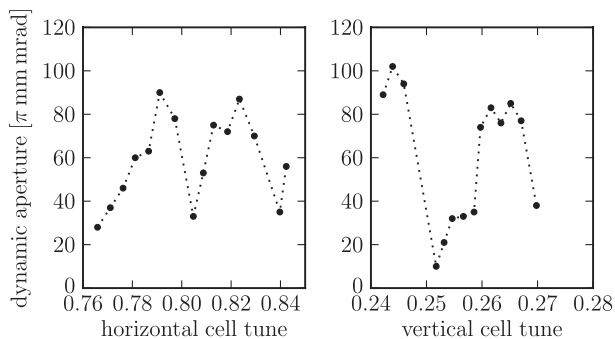

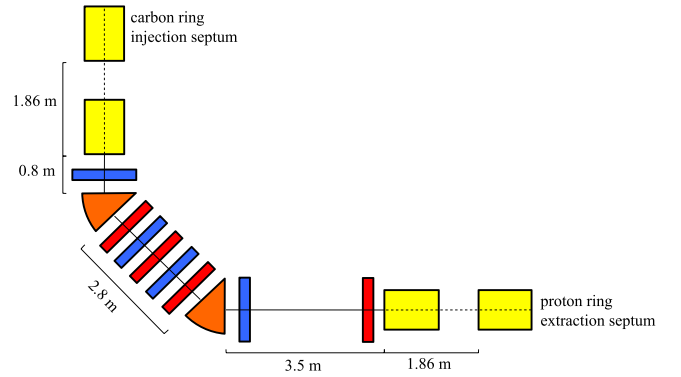FIG. 13.　Dynamic aperture vs (left) horizontal cell tune (ν_x), (right) vertical cell tune (ν_y).

FIG. 14.　Layout of the matched transfer line for C^{6+} ions from the proton to the carbon ring. Vertical bends are shown with dashed lines, yellow magnets bend in the vertical plane, orange dipoles bend in the horizontal plane, red rectangles are focusing quadrupoles (in the horizontal plane), and blue rectangles are defocusing.

low energy C^{6+} ions from the proton ring will be extracted at an angle of approximately 30° and the transfer line will need to approach the carbon ring at an angle which is sufficiently large to avoid the edge of the magnet cryostat, which is assumed to be 30°. A transfer line from the proton ring to the carbon ring has been designed matching the beam optics of both rings (see Fig. 14). This design allows the proton ring to be placed within the carbon ring, without a vertical displacement between the rings. The variable energy extraction system and beam transport for protons uses the same extraction septum as the carbon beam. To accommodate the FFAG optics of the proton transport to

TABLE VI.　Proton to carbon ring transfer line parameters. S1, S2, VB1, and VB2 are vertical bends; HB1 is a horizontal bend; all dipoles and all quadrupoles are of the same length; QF (QD) are focusing (defocusing) in the horizontal plane, and there are four different quadrupole doublets in the transfer line.

Parameter	Unit	Value
Septum bend angle (S1, S2)	mrad	640
Vertical bend angle (VB1, VB2)	mrad	640
Horizontal bend angle (HB1)	mrad	785
Bending magnet length	m	1
Quadrupole magnet length	m	0.2
Drift 1 length (D1)	m	1.0
Drift 2 length (D2)	m	0.3
Drift 3 length (D3)	m	2.5
QF1	m^{-2}	5.47
QD1	m^{-2}	−2.27
QD2	m^{-2}	−14.67
QF2	m^{-2}	13.57
QF3	m^{-2}	10.0
QD3	m^{-2}	0.08
QF4	m^{-2}	1.39
QD4	m^{-2}	−2.08

the treatment rooms, the transfer line is designed with a long horizontal drift section soon after extraction from the proton ring. It is envisaged that the beginning of the proton transport line could be integrated into this drift space. The main parameters of the proton to carbon ring transfer line design are given in Table VI.

V. MAGNETS

The PAMELA lattice design requires a magnetic field which is similar to the scaling law of Eq. (1), which can be decomposed into an infinite number of multipoles, although multipole components higher than decapole are not considered, which breaks the scaling law.

The lattice is made of triplets; in the proton ring each F and D magnet has a nominal length of 0.314 m, with a short straight section of 0.314 m in between. For the carbon lattice the magnet and short drift length increases to 0.633 m (see Fig. 15. It is assumed that the magnets can extend into the short straight section if necessary.

The path of the particle through the triplet is not straight but curved (see Fig. 16 which shows schematically the position of the F and D magnets in red and green, respectively). It is clear that the scalloped path of the individual particles means that the bore of the magnets has to be somewhat larger than estimated from the particle orbit excursion. This is particularly the case for the D magnet if the magnets are aligned on a straight line as shown in Fig. 16; not only is the bore larger, but also a higher magnetic field has to be generated as the magnitude of the magnetic field B increases for positive x. This can be partially remedied by offsetting the D magnet indicated by the arrow in Fig. 16; offsetting the D magnet leads to an easier magnet design due to the smaller bore and the lower overall magnetic field but the mechanical design and cryostat assembly is more complicated due to the dogleg shaped beam pipe. For the carbon lattice, which is more demanding than the proton lattice in terms of magnetic field and magnet aperture, only an offset solution is a realistic option; for the proton lattice a non-offset solution was chosen.

Tracking studies show a stable working point for the proton lattice for a k value of 38 at a reference orbit of 6.25 m. B_0 is 1.86 T and -2.32 T for the F and D magnet, respectively. For carbon the carbon lattice B_0 is 2.261 and -2.75 T for the F and D magnet, respectively. R_0 is 9.3 m
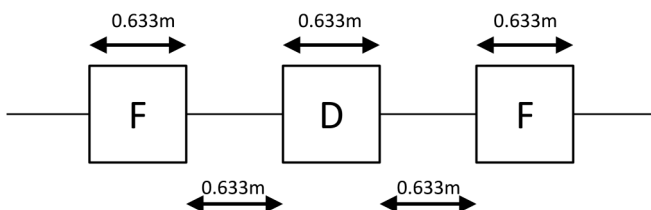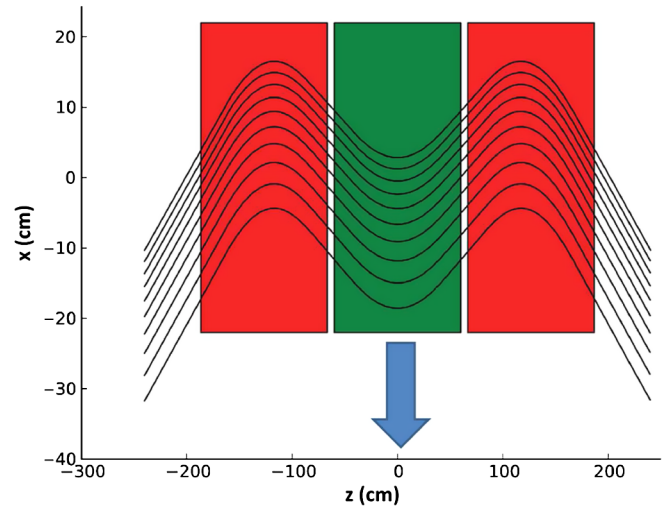

FIG. 16. Typical particle traces through the PAMELA triplet; the F and D magnets are indicated schematically by the red and green boxes, and the blue arrow shows the direction in which the D magnet must be displaced for the offset solution.

and the k value is 39. Equation (1) defines only the shape of the vertical magnetic field whereas important for the magnet design is the field experienced by the particles, particularly the minimum and maximum radius of the particles has to be determined. This was done using tracking studies with the code ZGOUBI [24]; an example is shown in Fig. 17, which shows the magnetic field the magnets have to produce in comparison to the scaling field. The required field is then produced by fitting an nth order polynomial to the scaling law,

$$B_y(x) = \sum_{i=0}^{n} a_i x^n, \qquad (4)$$
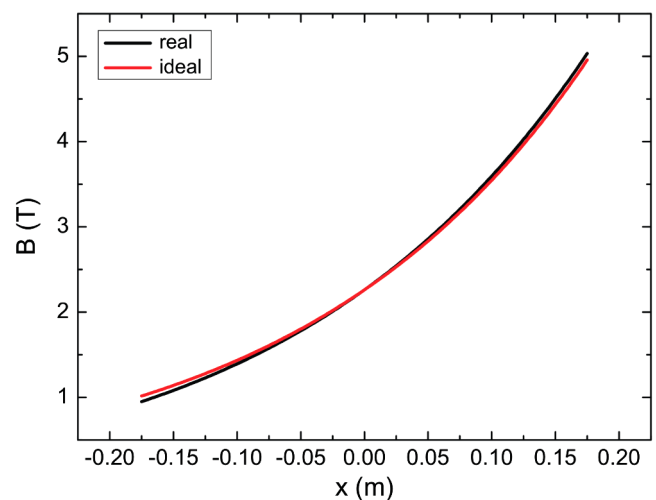

FIG. 15. The carbon lattice.

FIG. 17. A typical magnetic field using the scaling law in black, with the red curve highlighting the part experienced by the particles.
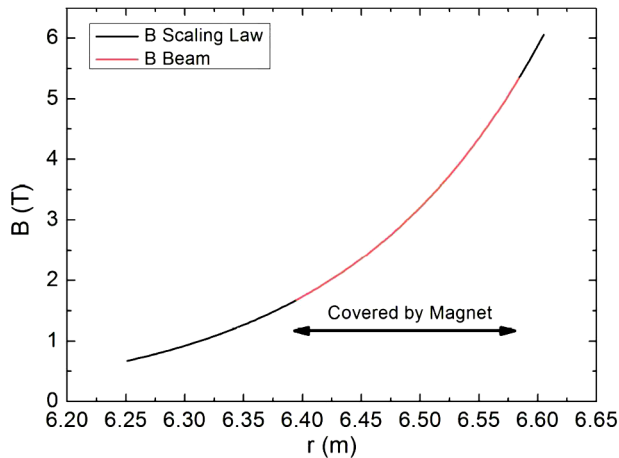
FIG. 18.   Vertical magnetic field of the carbon F magnet, comparing the ideal scaling law with the real magnetic field. For tune stabilization (see text) the quadrupole component was increased by 4.5% and the sextupole component by 2%. The octupole and decapole components were decreased by 4% and 25%, respectively.

where a_i are the polynomial coefficients and x is the horizontal position. The required magnetic fields for the protons F and D magnets are given in [26]; those for the carbon magnets are shown in Fig. 18.

The need for including multipoles up to decapole can be demonstrated by determining the local k value, which is defined as

$$k_{\mathrm{local}} = (r/B)(\mathrm{d}B/\mathrm{d}r). \qquad (5)$$

The result is shown in Fig. 19. The theoretical ideal is that of a constant local k value. As shown, without decapole field component the local k value changes by about 8%; with a decapole field component the variation is much smaller (about 1%). The implications are not fully understood, but this figure and results from tracking studies
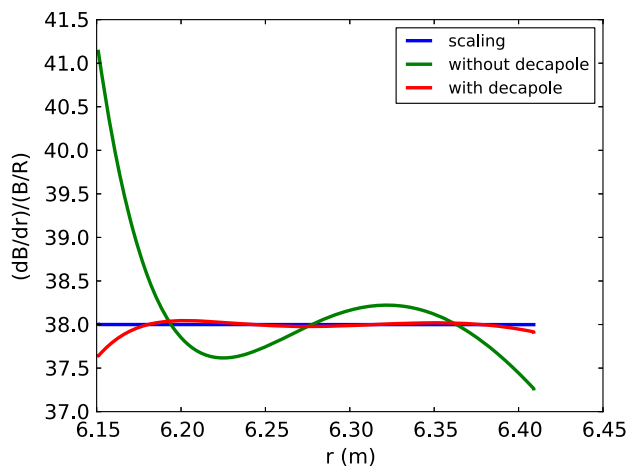

FIG. 19.   The local k value with and without decapole field component.

indicate that the decapole field is essential and therefore was considered in all magnet designs.

The magnets for the proton lattice are discussed in [26]; therefore the magnet design for the carbon lattice is discussed in detail. In terms of field quality it is assumed that the integral value of the magnetic field $\Delta B/B$ should be better than 10^{-3}.

A. The magnet design concept—helical coils

For PAMELA a purely superconducting solution was adopted; superconducting coils are in general capable of providing the necessary fields and have advantages in terms of stability and long-term running costs.

PAMELA requires combined function magnets with multipole components up to decapole. It is well known that an ideal multipole field can be created by a so-called cosine-theta current density distribution, where

$$J_z(\theta) = J_0 \cos(n\theta). \qquad (6)$$

In this equation θ is the azimuthal angle and n the multipole order ($n = 1$ for dipole, $n = 2$ for quadrupole, ...). J_z is the current density in the longitudinal (beam) direction. The required magnetic field can therefore be created by separate coils, each producing one multipole. It is also possible to create all multipoles with a single coil, which is the approach adopted here. The advantage is that only one pair of current leads is necessary, which greatly reduces the heat leak and thus the cooling power. Trim coils, producing pure multipole fields, may be added to fine-tune the field after assembly.

The magnets represent a significant challenge in that they have to be short high-field coils with an aspect ratio of about 2:1 (coil length divided by coil bore). A technique which is referred to as tilted solenoid or double-helix technology is employed, the principles of which were already established in the 1970s [27]; more recent work is discussed in [28].

The double-helix technology can be seen as a special variant of a cosine-theta magnet. The geometry of the helix in 3D Cartesian coordinates is described by the following equations:

$$x(\theta) = R \cos(n\theta), \qquad (7)$$

$$y(\theta) = R \sin(n\theta), \qquad (8)$$

$$z(\theta) = (h\theta/2\pi) + [R/\tan(\alpha)] \sin(n\theta). \qquad (9)$$

θ is the azimuthal angle, R the coil radius, h the pitch and n the multipole order, and α is the tilt angle of the solenoid, namely, the angle between front surface and the symmetry axis. The technique is called double-helix technology as two helices are always required per multipole or combined function magnet, with one helix nested inside the other. The second helix follows the same logic as the first, except

that the current flows in the opposite direction and the tilt angle is negative. Combined function fields can be obtained by introducing an additional parameter ε, which defines the ratio of the different multipoles. In the z direction the equation then reads

$$z(\theta) = (h\theta/2\pi) + [R/\tan(\alpha)]\sum_n \varepsilon_n \sin(n\theta). \quad (10)$$

It can be shown that when superimposing the two helices the direction of the current densities produce a pure cosine-theta current density distribution. A direct consequence is that the double-helix technology (in theory at least) is an almost perfect approximation of a cosine-theta magnet. The coil ends of a helical coil are not artificial structures but a natural extension of the straight section of the coil, which also contribute to the useful field.

The double-helix concept has been extended to a four coil concept to eliminate higher order components, as discussed in [26].

Helical coils have another advantage in comparison to ordinary cosine-theta magnets, which is their flexibility. Equation (10) suggests that each layer of a helical coil can generate only one designed multipole or a combination of multipoles. However, the equations also allow a single helical layer (and thus an entire double or quadruple helical coil) to generate a different multipole field at different longitudinal positions. In an ordinary cosine-theta magnet this is difficult to realize, as the number of constant current density blocks increases with the multipole order, and so additional wires of superconductor would have to be introduced, which is inelegant. For helical coils there is almost no issue—it is possible to vary the strength of individual multipoles by changing the value of the relevant ε_n, as shown in Eq. (10)

B. Magnet design

The magnet design was carried out using OPERA 3D from Vector Fields (Cobham) [29]. As no nonlinear materials are present, the magnetic fields can be evaluated using the Biot-Savart law. Table VII shows the results of the design process for the carbon ring offset solution. The solution is suitable for both the F and the D magnet (with opposite polarities). The design was carefully optimized in order to minimize the peak magnetic field on the wire while maintaining the desired performance.

As shown in Table VII, each multipole has multiple double layers, necessary to reduce the peak field on the wire, as each layer is exposed to the field of subsequent layers. Since there is a substantial solenoidal field, subdividing the coil in radial direction leads to a reduction of the solenoidal component between layers ($\sim 1/n$).

An important parameter for the helical coils is the tilt angle α. In general, it is advisable to choose a low tilt angle, as this means that more of the current flows in the longitudinal direction [$\cot(\alpha)$]. However, choosing a

TABLE VII. Carbon magnet designs—offset solution.

	Unit	F & D
ε_1		0.6152
ε_2		0.2863
ε_3		0.0803
ε_4		0.0162
ε_5		0.0020
R_{inner}	mm	175
R_{outer}	mm	221.2
Length	m	0.972
Pitch	mm	2
Number of turns		400
Tilt angle	°	60
Number of double layers		10
Wire radial thickness	mm	1.3
Wire axial thickness	mm	17
Gap between layers	mm	1
Average current density	A/mm^2	468
Peak field wire	T	4.7
Temperature margin	K	1.2
Current	A	860
Magnetic energy	kJ	440
Inductance	H	4.2

high tilt angle means that more turns can be wound in a given space, which increases the performance. The situation is further complicated by the fact that an important design parameter is the peak field on the wire, which not only depends on the desired field of the multipole but also on the unavoidable solenoidal field. The optimum tilt angle for PAMELA is between 50° and 65°. Figure 20 shows examples of the peak field on the wire for the D magnet for the carbon lattice; only the 4th layer of each coil is shown.
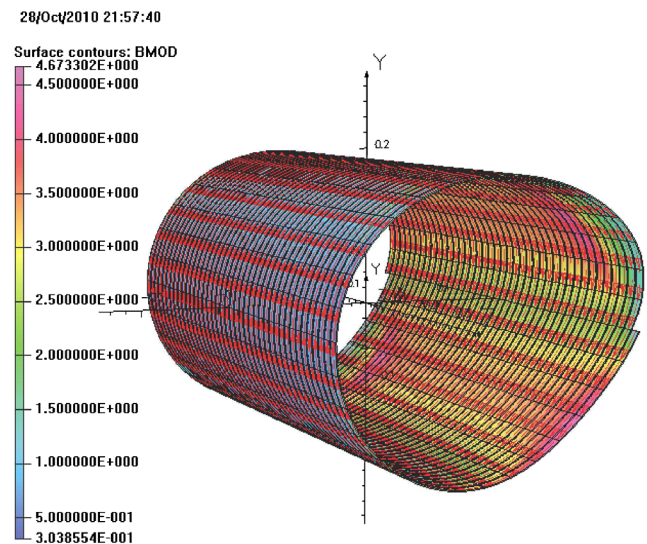

FIG. 20. Peak magnetic field on the wire of the D magnet for the carbon ring for the 4th layer from the center.
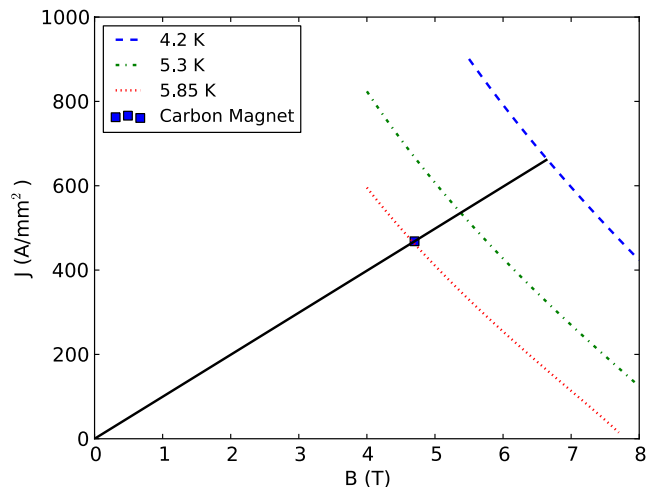
FIG. 21.   Load line of the carbon F/D magnet.

A 54 filament standard Nb-Ti conductor (F48) from Bruker [30] was chosen for this magnet. The wire dimensions are 1.79×1.17 mm^2 with insulation (1.68×1.09 mm^2 bare); the Cu:Sc ratio is 1.35:1. The copper to superconductor ratio was chosen to maximize the temperature margin. Figure 21 shows the load line of the magnet.

To correct tune drift the dipole component in each magnet of the triplet was varied, then the quadrupole and so on. Each optimization was targeted at improving the maximum tune drift. The focus was here on correcting the horizontal tune drift; the vertical tune drift, which is more susceptible to field shapes, is corrected by varying the strength of the dipole and quadrupole along the length of the magnet. The first and last 80 mm of the dipole and quadrupole of each magnet run at 75% performance, whereas the center runs at 100% performance. It was found that this flattened the tune sufficiently. The horizontal tune drift is smaller than 0.33 and the vertical tune drift is smaller than 0.258.

1. Field quality

The target field quality $\Delta B/B$ for the magnets is of the order of 10^{-3}. Helical coils in general have a very competitive field quality in theory due to the better approximation of the ideal cosine-theta current density distribution. The field harmonics, which demonstrate the field quality, are shown in Table VIII, which shows the coefficients for the normal and skew field components at a radius of 100 mm. The field can be calculated using the following equation:

$$B(x + iy) = \sum_{n=1}^{\infty} (B_n + iA_n)\left(\frac{x + iy}{R_r}\right)^{n-1}. \quad (11)$$

The table emphasizes that apart from the desired field components (dipole to decapole) almost no higher order

TABLE VIII.   Field harmonics of the PAMELA carbon magnet.

	B_n	A_n
1	1.437×10^{0}	-7.731×10^{-12}
2	6.771×10^{-1}	-6.22×10^{-12}
3	1.460×10^{-1}	-2.08×10^{-12}
4	2.02×10^{-2}	1.03×10^{-11}
5	1.644×10^{-3}	-3.80×10^{-12}
6	8.39×10^{-13}	2.473×10^{-12}
7	2.597×10^{-13}	-1.102×10^{-11}
8	9.238×10^{-14}	-1.93×10^{-11}

multipoles or skew multipole components are present. On average the field quality is between 10^{-5} and 10^{-6}. In practice the field quality will be determined by the mechanical tolerances; a random misalignment of ± 0.1 mm is sufficient for the envisaged field quality. It should be emphasized here that small deviations in the absolute field can be compensated by trim coils, which may be added to the design.

VI. RF SYSTEM

The primary challenge of the PAMELA beam acceleration system is achieving a repetition rate of 1 kHz over an energy range of 31 to 250 MeV for the proton ring and from 68.8 to 440 MeV/u for the carbon ring, more than an order of magnitude higher than that achieved by existing rapid cycling proton synchrotrons. Spot scanning is carried out using constant bunch intensity—"multibunch painting" and a high repetition rate is required to achieve uniformity of dose field and sufficiently high scanning rate simultaneously [31]. The required intensity is quite low at a maximum value of 10^7 protons/pulse, compared with modern synchrotron intensities of greater than 10^{13} protons/pulse so that beam loading and space charge effects are unimportant. The low and variable β of the 31–250 MeV proton beam results in a 2.4:1 frequency swing for the proton rf. A consequence of the high repetition rate of 1 kHz is that the rf system must accelerate the particles in less than 1 ms. Beam loading of the rf is negligible with a maximum, mean circulating current of 70 μA, but significant rf power is required for the proposed ferrite-loaded cavities. The rf parameters for proton acceleration are outlined below, followed by an initial appraisal of the requirements for C^{6+} ion acceleration.

The energy range of the proton ring is 31–250 MeV, necessitating an average energy gain of at least 74 keV/turn for acceleration in less than 1 ms. However, if an equivalent period is allowed for the rise and fall of the rf then the required energy gain rises to 148 keV/turn. Since the rate of change of frequency is high compared with current operating accelerator rf systems (by a factor of at least 10) a symmetric rise and fall of the frequency was chosen.

TABLE IX.   Requirements of PAMELA rf system.

Item	Unit	Value
Frequency for $h = 1$(inj/ext max)	MHz	1.92/4.56
Repetition rate	kHz	1
Energy gain/turn	kV	100
Number of cavities		Up to 8
Cavity length	m	<1.2
Cavity aperture	m	0.2

The proposed magnet lattice has 12-fold symmetry and at least two long straight sections are required for the single-turn injection and extraction, so that up to eight straight sections are available for rf cavities and additional instrumentation. The geometric constraints on the rf are the 1.7 m length of the straight sections and the horizontal aperture required for the orbit excursion of 0.17 m and beam diameter. Vertical aperture is required only for the beam vertical size. To leave room for beam diagnostics and vacuum pumps, the cavities should ideally be less than 1.2 m in length and provide a horizontal aperture of more than 0.2 m. The requirements of the radio-frequency accelerating system are summarized in Table IX.

Several rf schemes were considered: (i) harmonic number jumping narrow bandwidth high Q cavities; (ii) induction cavities; (iii) broadband magnetic alloy (MA) cavities; (iv) ferrite-loaded rf cavities. However, after considering the advantages and disadvantages of each scheme, it was decided to concentrate on the design of ferrite-loaded rf cavities.

A. Ferrite-loaded rf cavity system

Ferrite-loaded cavities use well-established technologies and are designed to operate in a resonant regime, thus decreasing drive power requirements [32]. The power dissipation of an rf cavity is expressed as

$$P = V^2/(2\omega QL), \tag{12}$$

where V is the peak rf gap voltage, ω is the rf angular frequency, Q is the cavity quality factor, and L is the cavity inductance. In terms of power dissipation, and hence eventual power consumption, a high Q cavity is desirable and the limited space for the cavity forces the choice of a high frequency. However, ferrite materials have higher losses at frequencies above 50 MHz and wide bandwidth rf power becomes more difficult to achieve above 50 MHz. For these reasons harmonic number 10 was selected for the rf system. Drift tube and resonator options were considered but the current design of the PAMELA rf cavity is similar to the second harmonic rf cavity developed for the ISIS spallation neutron source at the Rutherford Appleton Laboratory [33], with the operating frequency substantially increased to 19.2–45.6 MHz. This enables a two-gap cavity to fit comfortably within the lattice straight sections and to

support gap voltages of up to 15 kV peak. A simplified equivalent circuit and outline structure are shown in Fig. 22.

The gap voltage is determined by the number of cavities and the allowed acceleration time of 0.5 ms. The 15 kV value is comfortably achieved with well-established vacuum tube (power tetrode) technologies. In a medical machine, reliability and to some extent redundancy in the acceleration system are of paramount importance. A specific drawback of such cavities is the need to provide a DC tuning current input, to achieve resonance over the 2.4:1 range of operating frequencies. This will require a significant (kA) drive current and careful characterization of available ferrite materials. The power tetrode drive amplifiers will be situated adjacent to the cavity since the operating impedance must be maximized. Nevertheless, provided suitable ferrite materials can be identified, as described below, such a cavity design will deliver the required performance, efficiency, and reliability. The proposed baseline design is shown in Fig. 23. The overall cavity length, including a vacuum pumping port (or space for additional beam diagnostics), is 1.1 m, flange-to-flange distance, well within the design requirements.
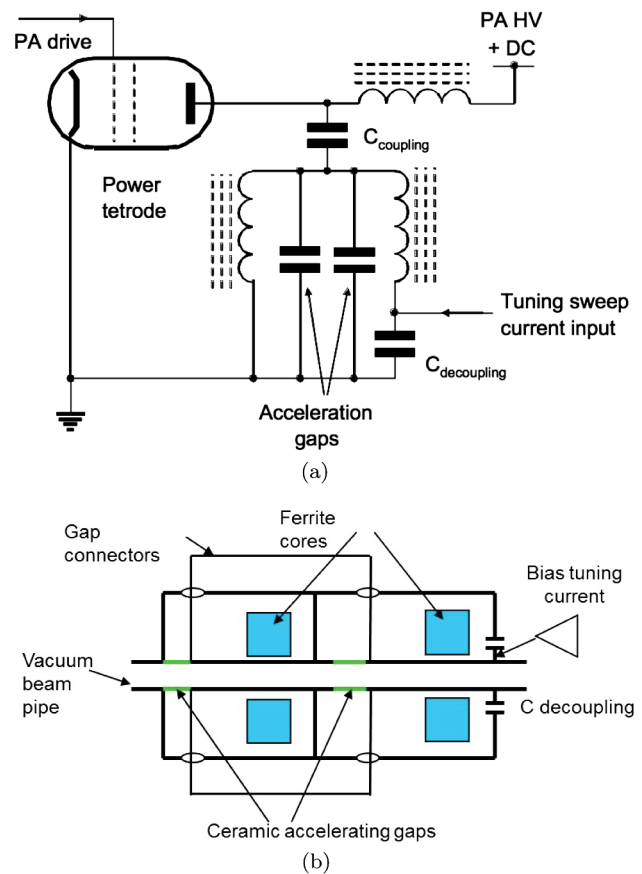

FIG. 22.   (a) Equivalent circuit of dual-gap cavity and associated tetrode power amplifier (PA), with core biasing current input and (b) schematic of cavity design.

K. J. PEACH *et al.*

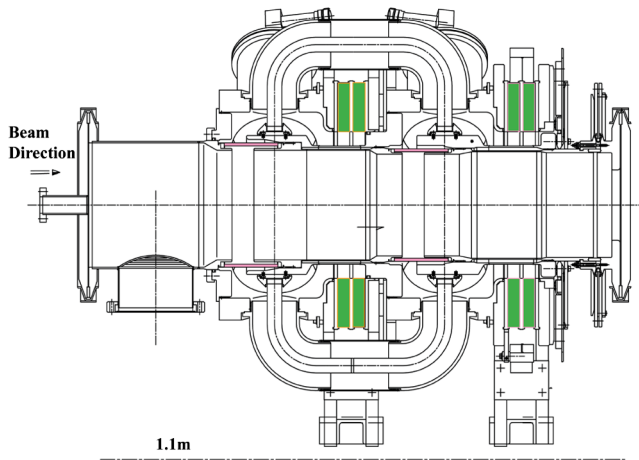Phys. Rev. ST Accel. Beams **16,** 030101 (2013)

FIG. 23. Side view of planned ferrite-loaded rf cavity.

Several NiZn ferrite materials are commercially available, offering values of static Q of the order of 100, with appropriate values of initial permeability. Some of these have been bench tested at very low powers. Currently, the most promising material is Phillips 4E2 ferrite [34], though measurements of the initial permeability, μ_i, seemed significantly higher than that specified by the manufacturer (as specified in the catalogue of the company: ~25). The material specification is shown in Fig. 24, where the real and imaginary components of the complex initial permeability are plotted against operating frequency. For completeness, the temperature and magnetization characteristics are also shown [35] in Fig. 24. The static values of Q will not be achieved when the cavity voltage and resonant frequency are changed rapidly during the acceleration cycle. However, if a Q of 20 or 60 is assumed then some power estimates for the rf system can be obtained for $\Delta E/\text{turn} = 144$ keV with ϕ_s $60°$–$70°$ and acceleration time 0.44 ms. The gap voltage, drive current, and power as a function of operating frequency can be derived and these are plotted in Fig. 25.

As mentioned in the Introduction, a consequence of a fast-cycling machine is the inevitable need for high rf drive power. Under the conditions discussed above, the current and power required at different frequencies, and hence time, can be calculated; these data are shown in Figs. 26 and 27.

These plots indicate that for a Q of 20 a significant peak power will be required. In the proton ring, a total of 16 gaps will be used, operating at a mean power of 65 kW during the acceleration cycle, equivalent to half of this power if the rf is turned off during the 0.5 ms recovery to the start frequency. The total cavity power estimate for the 16 gaps will thus be 520 kW; note that this is similar to the power requirements of current charged particle therapy facilities, which range from 200 kW to 3 MW, depending upon the manufacturer, the type of accelerator, and the number of treatment rooms. Clearly, if higher Q value can be obtained
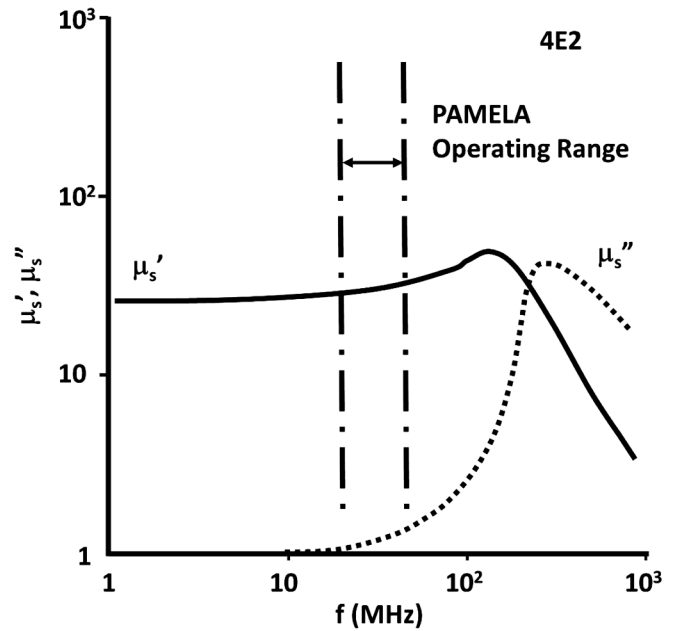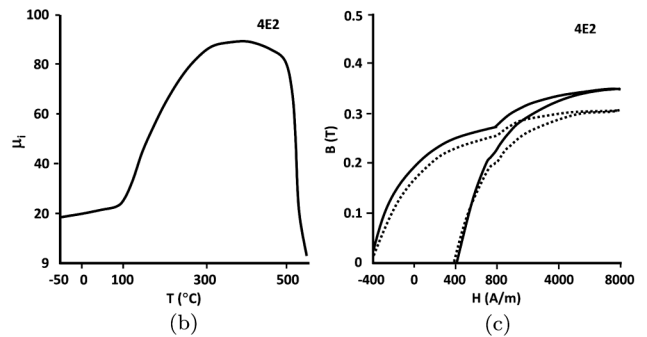
FIG. 24. Material properties of NiZn ferrite 4E2. (a) Frequency dependence of complex permeability. (b) Temperature dependence of imaginary part of permeability. (c) The magnetic flux density B as a function of the magnetic field strength H.
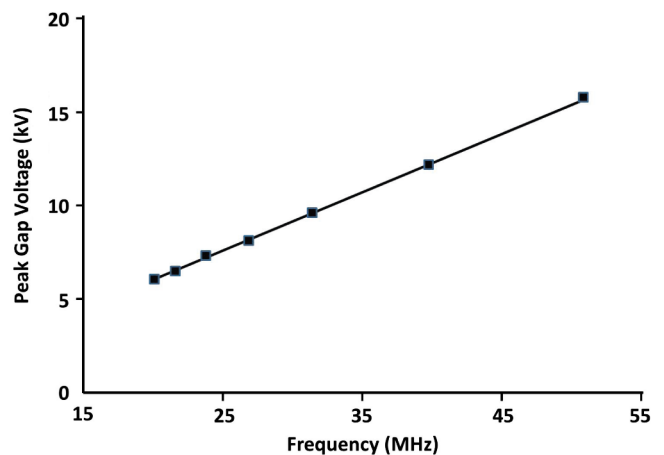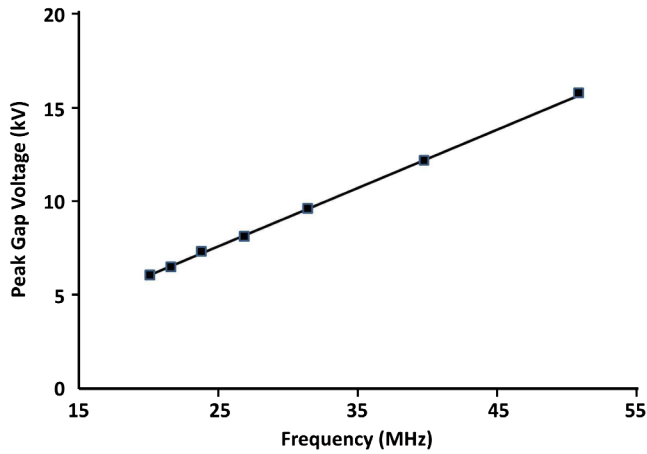

FIG. 25. Frequency dependence of cavity gap voltage.

FIG. 26.   Frequency dependence of cavity gap current.
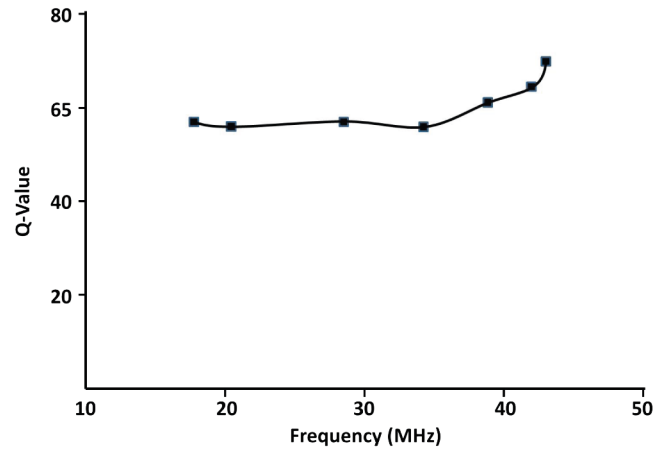

FIG. 27.   Frequency dependence of cavity power consumption.

then there will be significant saving in power. Initial low power measurements indicate that a Q of 60 may be feasible and this would reduce the cavity rf power requirements by a factor of 3.

B. Ferrite property measurement

The estimation of cavity performance is based on the Q value assumptions of the ferrite core. As a first step of the development, the properties of candidate ferrites were measured. From the initial tests Philips 4E2 ferrite was selected for more detailed measurement. The frequency dependence of the Q values was measured on a small core sample of 4E2 under biased conditions; Fig. 28 shows that the Q value of about 60 was obtained on this small sample over the entire operation frequencies, and the value is well above the requirement. With this measured Q value, the hardware requirements would be considerably reduced, supporting the feasibility of the cavity, although the Q value must be confirmed in a real cavity under the variable frequency and voltage condition.

FIG. 28.   Measured frequency dependence of Q value of 4E2 under biased condition.

C. Extrapolation to carbon ring

Initial consideration of an rf system for C^{6+} acceleration using the proton ring and a second ring of radius 9.3 m with 12 super periods leads to the following parameters assuming the C^{6+} rigidity is made equal to the proton rigidity in first ring. The lower frequency of the proton rf system would need to drop to 16.7 MHz due to the increased frequency swing for C^{6+}, but this seems the easiest option, making the rf swing from 16.7–45.8 MHz.

The energy gain for the carbon in the second ring is double the energy gain in the first ring for protons and of course the charge-to-mass ratio has halved so the acceleration time goes up to 1.7 ms. In order to achieve the 0.5 ms acceleration time, the voltage per turn would need to increase by a factor of almost 4. With the available space this looks difficult; one option is to use the same rf design in both rings thus saving on manufacturing costs and spares, but the cycle time of $(1.7 + 0.5)$ ms may be considered too long.

TABLE X.   Summary of parameters of the rf cavity.

		Proton Ring (protons)	(C^{6+})	C^{6+} Ring
Injection energy	MeV/n	31 MeV	7.9	68.8
Extraction energy	MeV/n	250	68.8	440
Harmonic number		10	17	10
Injection rf frequency	MHz	19.2	16.7	19.2
Extraction rf frequency	MHz	45.6	45.8	39.1
Frequency ratio		2.4	2.8	2.0
Number of two gap cavities		8	8	8
Voltage/gap	kV	10	10	10
Maximum voltage/turn	kV	160	160	160
Maximum voltage/turn	kV/n	160	80	80
Assumed ϕ_s	°	60–70	60–70	60–70
Acceleration time	ms	0.44	0.44	1.72

Trapping in the rings requires further study as some beam loss may occur in the carbon ring unless time is allowed to move the 45 MHz bunches towards the stable phase point for the 19 MHz. This, and aperture requirements, need further study. It should be noted that the 2.2 ms cycle time is still an order of magnitude shorter than most existing synchrotron sources. The parameters of the rf cavity are summarized in Table X.

The ubiquitous workhorse amplifier device at the low rf frequencies applicable to the current design is the power tetrode. Although a single-ended drive was shown in Fig. 22, a push-pull configuration may be more appropriate. Since there will be a total of eight cavities, such an approach would require 16 tetrodes. This issue has not been considered in detail here, as much will depend on availability of suitable tubes and their price-performance ratio. Although a single tube per cavity [e.g. the Thomson TH535 or EEV CW1603J2 (300 kW, 100 MHz)] can readily deliver the required power, the commercial production of high-power tubes has declined in recent years.

VII. ION SOURCES AND PREACCELERATION

The injection layout for protons and C^{6+} ions for PAMELA is shown in Fig. 1. The injection system uses a commercially available 31 MeV cyclotron for protons and a chain of elements for carbon ions including an electron cyclotron resonance (ECR) ion source, bending magnets and focusing solenoids, a radio-frequency quadrupole (RFQ), an interdigital H mode/crossbar H mode (IH/CH) structure and a stripping foil.

The injection energies for proton and C^{6+} beams into the FFAG rings of PAMELA are approximately 31 and 8 MeV/u, respectively. To achieve the same magnetic rigidity, to allow commissioning with protons, and to enable rapid switching between ion species, protons and carbon ions come from separate sources. The carbon ions are transported from the ion source into a preaccelerator via a low energy beam transport (LEBT), accelerated, and from there injected into PAMELA through a medium energy beam transport (MEBT). Part of the MEBT is shared with protons delivered from the cyclotron. There are two options for preaccelerating carbon, either accelerating C^{4+} ions from the ion source and stripping after the preaccelerator or accelerating C^{6+} ions all the way from the ion source; both options have been investigated. The

proposed system of proton and carbon ion sources and beam transports is illustrated in Fig. 29.

For carbon ions an electron cyclotron resonance ion source (ECRIS [36]) is used to produce C^{4+} or C^{6+} ions because of its high beam quality and beam current stability, with a stripping foil at the end of the RFQ if C^{4+} ions are used; both have been studied. It is possible to extract sufficient current with C^{6+} ions, which avoids the need for a stripping foil, and so this option is discussed below; details of the C^{4+} acceleration scheme can be found in [37]. The main difference between the two is the frequency of the RFQ (200 MHz for C^{4+} and 240 MHz for C^{6+}); the lower frequency of the RFQ for the C^{4+} ions favors the rod design. Depending on the injection scheme, a supernanogun or hypernanogun ECRIS can be employed for a multiturn or a single-turn injection scheme, respectively, or could be used for single-turn injection with a superconducting magnet [38]. Since PAMELA has a high repetition rate a single-turn injection is assumed, but a multiturn injection is not excluded. A spectrometer with collimators is used to separate the required ion from the mixture of C^{3+}, C^{4+}, C^{5+}, and C^{6+} ions.

A typical ECR ion source produces 12 keV/u C^{6+} with an extracting voltage of around 24 V, chosen from the requirements imposed by the Child-Longmuir law, and to avoid technical difficulties occurring for higher voltages. The Child-Longmuir law can be written as

$$J = (4\varepsilon_0 V_0^{3/2} \sqrt{2e/m})/(9d^2),$$

where J is the current density and V_0 is the extracting voltage at a distance d from the ion source, and e and m are the electron charge and mass, and ε_0 is the permittivity of free space. This current limit exceeds the requirement by more than 2 orders of magnitude. The total energies extracted are shown in Table XI, and the phase space plots are shown in Fig. 30. Because of the lack of measured input data for the simulation, and based on the beam energy considerations shown above, an initial particle distribution was produced to represent the beam extracted from the ion source. Typical beam parameters for carbon injection from an ECRIS are given in Table XII. The beam parameters strongly depend on the RFQ acceptance. The pulse duration is 506 ns and the design frequency is 240 MHz; the bunch distance inside the RFQ is therefore $1/(240 \times 10^6) = 4.16$ ns. Considering a sixth of the rf period
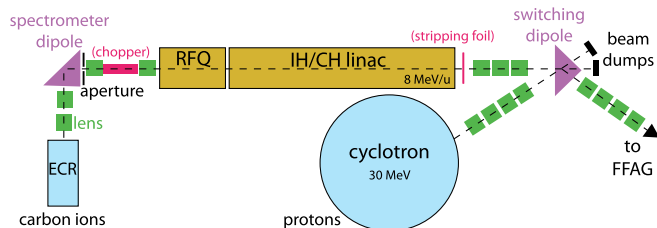

FIG. 29. The beam injection scheme.

TABLE XI. Ion source energies at extraction.

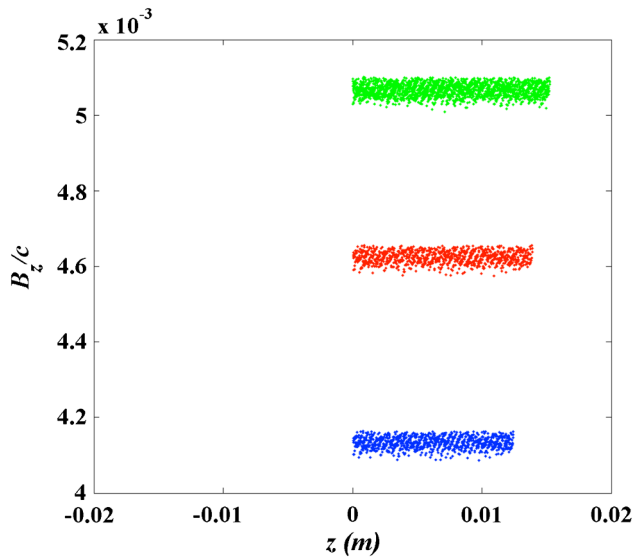| Ion charge	Extraction energy keV	Energy per nucleon keV/u
C^{3+}	$24 \times 3 = 72$	$72/12 = 6$
C^{4+}	$24 \times 4 = 96$	$96/12 = 8$
C^{5+}	$24 \times 5 = 120$	$120/12 = 10$
C^{6+}	$24 \times 6 = 144$	$144/12 = 12$

FIG. 30. Longitudinal velocities of C^{6+} (top), C^{5+} (middle), and C^{4+} (bottom) ions, immediately after the ECRIS. C^{6+} shows the highest kinetic energy applying the same extracting voltage, here 24 kV, to all species.

for acceleration (i.e. 60 out of 360), the bunch length would be 4.16 ns/6 = 0.694 ns accordingly. The number of bunches in the train can be approximately estimated to be (506 ns)/(4.16 ns) = 122.

The LEBT will transport the particles from the source to the RFQ. For carbon, the layout consists of four solenoids for transverse focusing and a spectrometer dipole to select the required charge state. Particle transport simulations for the proton and carbon injectors have been carried out using the General Particle Tracer software from *Pulsar Physics* [39] using the built-in elements. Two solenoids, each 0.25 m long, are positioned at 0.325 and 0.875 m from the ion source; the first solenoid transports the particles parallel to the axis and the second focuses them. After the charge-to-mass separation by the spectrometer, two more solenoids focus the beam into the RFQ. The spectrometer dipole bends the beam downward. The angles of the entrance and exit pole faces are taken to be 250 mrad. The parameters of the coils are shown in Table XIII.

Apertures 10 mm in radius before and after the spectrometer dipole ensure that only the ions in the necessary charge state are allowed to enter the preaccelerator. A full RFQ design requires optimization of the rod modulations

TABLE XII. Ion source beam parameters (emittances are normalized).

Parameter	Unit	Value
Beam radius	mm	2
Beam divergence	mrad	50
Beam emittances	mm mrad	0.25π
Beam pulse duration	ns	506

TABLE XIII. Solenoid parameters. Note that after the 90° spectrometer dipole, a change in the reference system takes place. The single-starred distances are measured from the ion source, the double-starred distances are measured from the spectrometer dipole.

Name	Current (A turns)	Inner radius (mm)	Outer radius (mm)	Width (mm)	Distance from reference (m)
Rectcoil 1	57000	50	100	0.25	0.325*
Rectcoil 2	40000	50	100	0.25	0.875*
Rectcoil 3	48000	30	80	0.25	0.250**
Rectcoil 4	105000	30	80	0.25	0.750**

to provide the correct bunching and acceleration for the specific particles and energies to be used for PAMELA. The simulations are based on the details of the RFQ for the front-end test stand (FETS) [40], and various scaling laws have been investigated to determine the changes required to produce a carbon RFQ. The FETS RFQ uses four vanes.

In the case of a rapid cycling FFAG like PAMELA (repetition rate more than 500 Hz), the use of C^{6+} is favorable. This not only has consequences for the rod modulation and resonator setup, but also a superconducting RFQ might be considered. In the simplest case, the time to fill an rf cavity can be approximated by the inverse of the frequency and the Q value of the cavity, $\tau \simeq Q/\pi f$. For a 240 MHz cavity with a Q value estimated to be roughly 1000, this filling time is of the order of 5 μs. The FFAG ring, on the other hand, has a revolution time of approximately 1 μs, and half filling the ring at injection (to leave space for kickers, etc.) will require a 500 ns pulse. This means that, at injection, the power will be dissipated for 10 times longer than needed to produce useful beam. Power losses would go down as the ratio of the Q value, giving a superconducting RFQ with a few orders of magnitude lower power losses than a normal-conducting RFQ; in a normal-conducting accelerator, nearly all the rf power is lost in the cavity. The duty factor overall is still small and the total power on average dissipated is reasonable, which implies a normal-conducting RFQ assumed to be a primary candidate. Nevertheless, a superconducting solution could have some advantages in terms of stability and should not be excluded beforehand.

TABLE XIV. Input parameters for C^{6+} RFQ simulations.

Parameter	Units	Value
Energy at start of RFQ	keV/u	12
Frequency	MHz	240
Length	m	2.4
Pole-to-pole voltage	kV	78
Beam current	μA	1
Beam divergence	mrad	−60
Beam emittance	mm mrad	0.25

TABLE XV.   Output results for C^{6+} RFQ simulations.

Result	Unit	Value
Mean energy at end of RFQ	keV/u	557
RMS energy spread at end of RFQ	keV/u	8
Transmission	%	99.2

As the power requirement is low, a wide-band rf amplifier can be used, and the RFQ frequency can be based on the best particle dynamics. The design parameters for a superconducting C^{6+} RFQ are summarized in Table XIV. These parameters are not the only working point, and further optimization of the design may alter these values, while maintaining the performance. The increased frequency of the RFQ favors a vane design. The Kilpatrick factor for this simulation is 1.64. The results of simulations are given in Table XV.

In general, the advantage of using a linac as the injector is the high current limit and the good transmission due to strong transversal focusing. The main disadvantages are the high investment costs and large space requirements. While the current limit exceeds the requirement for medical applications by at least a factor of 10, the achievable average electric field strength for acceleration of low beta ion beams is usually 3 MV/m; the high current available at low energies (1–5 MeV/u) makes them ideal candidates as an injector; this is relatively conventional technology.

The MEBT design assumes that proton and carbon ions would be independently produced and preaccelerated in a cyclotron and a linac, respectively. The main aim of the MEBT is to minimize the loss of current at injection. A switching dipole (SD) combines the two beam lines and transports both ion species to the injection point of the first PAMELA ring, where the beam matching into the FFAG injection requirements is also done. In some scenarios it may also be used to act on the longitudinal beam structure.

The SD bends the carbon and the proton beams through different angles, according to the ratio of the magnetic field integral and the magnetic rigidity in order to combine the two injection lines. The magnetic rigidity of carbon and proton are the same since the orbits and magnetic fields in FFAG ring are set to be the same; the length of the SD should also be kept approximately fixed.

To minimize the switching time between the proton and carbon operation modes, the common beam line for both proton and carbon species would not be tuned and the only element requiring a change of current would be the SD. This assumes the same optics in the part of the MEBT located downstream of the SD. However, the SD would have different focusing properties for two species as the deflection angles are not the same due to geometrical constraints.

The switching dipole needed to combine the proton and carbon beam lines gives extra dispersion which requires compensation. Horizontal dispersion matching is achieved
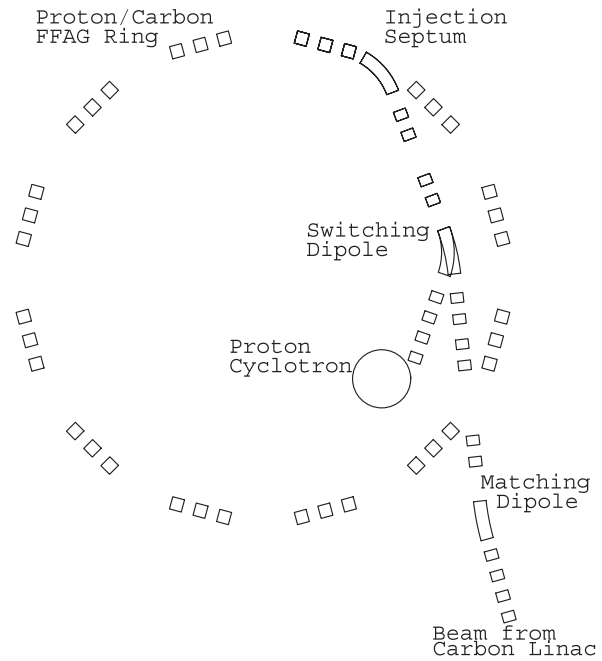

FIG. 31.   MEBT injection layout for PAMELA, based on a cyclotron inside the FFAG ring.

by choosing the phase advance between the SD and the septum. As the exact value of the dispersion function at extraction from the cyclotron is not yet known, a zero value was assumed, but this system should have enough freedom to match other values. In order to obtain enough flexibility in performing matching of optical functions, four quadrupoles are located downstream of the SD in the common proton/carbon part. A long drift section is also introduced
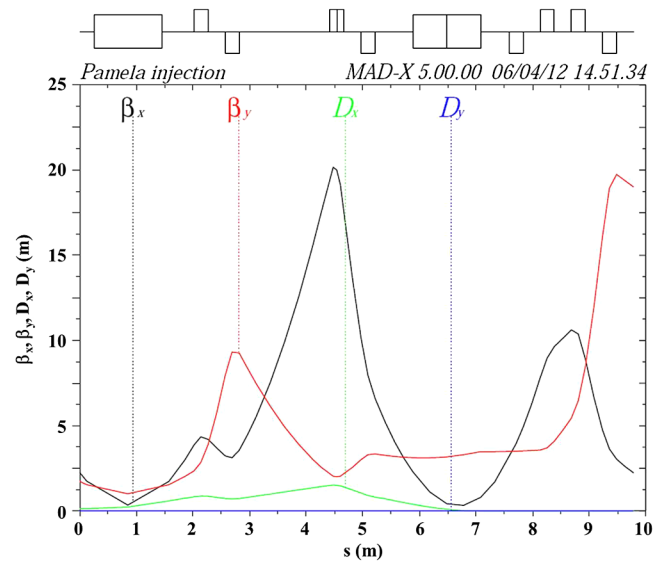

FIG. 32.   Beta functions and dispersion for the proton line shown in Fig. 31. The optics is shown in the inverse configuration, which means that the cyclotron is located on the right and the FFAG cells are located on the left.
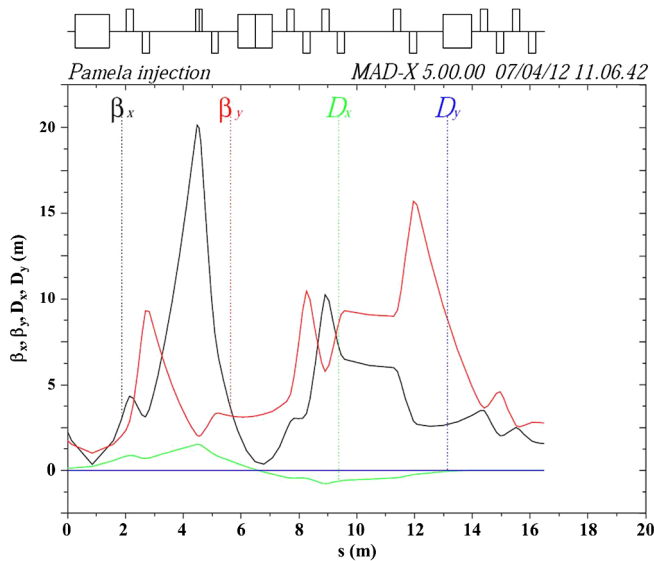
FIG. 33. Horizontal and vertical betatron functions in the carbon line obtained via MAD-X (again in the inverse configuration).

in this part of the MEBT, where a chopper could be located. For the betatron matching in the proton part, four quadrupoles are assumed upstream of the switching dipole. As the MEBT is designed such that only the magnetic field in the switching dipole would be changed when the proton/carbon operation modes are flipped, the dispersion matching in the carbon line requires an additional bending magnet. This is dictated by different deflection angles of the SD for proton and carbon beams. In addition, the sign of the edge angle on the upstream part changes sign, which changes the focusing properties in the vertical plane. This design simplifies a magnetic design of the SD, but makes the optical matching more demanding: separate sets of quadrupoles are used to perform the beam matching from the linac: four quadrupoles upstream of the matching dipole and six quadrupole magnets separated into three doublets between the dipole and the switching dipole.

In the case of the proton beam transport line there are four quadrupoles before and another four after the switching dipoles (see Fig. 31). Each quadrupole is 0.25 m long. Using this chain of elements a matched solution between the cyclotron and the FFAG has been obtained. The optics of the matched solution, found by MAD-X [15], is shown in Fig. 32. The matched solution for the carbon transport line is shown in Fig. 33.

VIII. INJECTION AND EXTRACTION

The challenge in PAMELA is variable energy extraction in a fixed field accelerator, since the horizontal orbital shifts as the energy changes. In addition, spot scanning treatment requires that the energy has to be capable of being varied by 40 MeV in much less than 1 s. The requirements of a beam extraction system of the proton ring are

TABLE XVI. Requirements of beam extraction system of proton ring.

Parameter	Unit	Value
Extraction energy	MeV	70–250
Energy width per treatment	MeV	40
Repetition rate	kHz	1
Beam size (unnormalized)	mm mrad	10π
Rise time	ns[a]	100

[a]The minimum revolution period is 220 ns.

summarized in Table XVI. The rise time requirement (100 ns) assumes that half of the revolution period is available. A detailed discussion of this is given in Sec. VIII A 1.

Four options were considered for variable energy extraction: (i) horizontal extraction with a full-coverage kicker; (ii) horizontal extraction with a C-shaped fixed kicker; (iii) horizontal extraction with a C-shaped movable kicker; and (iv) vertical extraction with a full-coverage kicker. The third option requires that the kicker and septum positions to be adjusted after each treatment, making the system complicated and lengthening the time between treatments, compared with the other options; however, this option is easiest in terms of the kicker specification for horizontal extraction. Nevertheless, detailed studies showed that vertical extraction with full horizontal coverage kicker was the most practical solution.

There are at least three advantages of the vertical extraction scheme.

The weaker field and voltage of the power supply.—For a kicker of 1 m the required field and power supply voltage are 0.06 T and 30 kV. This is sufficiently below the saturation limit of an ordinary fast ferrite (around 0.3 T) and tolerable voltage of pulsed power supply (80 kV). Considering the rigidity of carbon ring (factor of about 2.60 in magnetic rigidity), the required field and voltage are 1.6 T and 78 kV, respectively, still below the achievable level, even if a traveling wave kicker is employed.

Good matching with FFAG transport line.—In FFAGs, the horizontal orbit position is a function of momentum. Thus, in vertical extraction, the beam is extracted by keeping the momentum-position relation unchanged, directly connecting to the FFAG transport, with some optical matching elements.

The kicker and septum can be used for injection.—For the proton lattice, the optical functions α, β, and ν are almost flat over the entire energy range; the same scheme works for both extraction and injection. Considering the momentum and revolution period, injection is much easier. In addition, the order of the septum and the kicker for extraction is opposite to that for injection but the field direction is the same, so that if necessary, the extraction kicker can be also used as the injection kicker, providing one additional free straight section for other purposes.
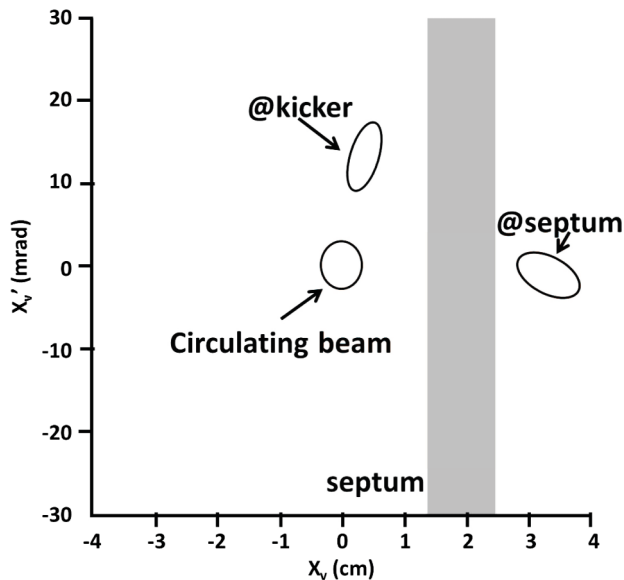
FIG. 34.   Phase space motion for vertical extraction.

Tracking simulations were carried out for vertical extraction. Figure 34 shows the vertical phase space motion of a beam kicked with the bending power of 0.06 T m, showing that sufficient orbit separation is obtained. Vertical extraction seems feasible from beam dynamics and hardware considerations. The vertical motion is strongly influenced by the nonlinear field as well as the horizontal motion, and the beam dynamics study suggests that the vertical dynamic aperture is smaller than the horizontal one. For the final specifications, tracking studies with an analytical field model is not sufficient and a similar study with a realistic 3D field is needed.

A. Kicker system

1. Pulse shape

In PAMELA, fast injection and extraction with kicker magnets are needed and two options have been considered. The first employs a half sine wave, well suited to short bunch injection/extraction and providing a higher voltage than the traveling wave option. The traveling wave option forms a flattop and can be applied to a longer bunch; due to the nature of formation of the flattop, only half the power supply voltage is available to generate field, although injection with a flattop allows dynamic intensity modulation by including an active chopper in the injection line. In the case of rf acceleration with a harmonic number of 10, five buckets can be filled with beam if the width of the flattop is equal to the revolution period. By changing the number of buckets filled with beam, intensity modulation of a factor of 5 can be achieved, enhancing the effective repetition rate by about a factor of 4. The requirements for both options are discussed.

In fast injection the orbit separation at the septum is corrected with the kicker, which means that the kicker field

should be excited during the injected beam traversal of the kicker and vanish before the bunch reenters the kicker after one revolution. As a result of this, the fall time requirements for the two options differ. For the half sine wave case, about 80% of the revolution period is available for fall, so that the fall time is 430 ns if the harmonic number is 10. For the traveling wave case, assuming that the flattop should cover the half of the revolution period, the fall time should be below 250 ns.

The field error at the kicker (the residual field after one revolution and field fluctuation during the kicker excitation) results in injection errors and excites finite amplitude betatron oscillations. The field error can be estimated such that the remaining amplitude is sufficiently small. The orbit separation at the septum is typically 30 mm in vertical injection/extraction. For example, a net field error of 10% excites betatron oscillations of 9π mm mrad (unnormalized); the typical $\beta_\nu \sim 1$ m. Recalling that final beam size for spot scanning is typically 3×3 mm^2 and that resonances are not crossed, a field error of 10% is the maximum acceptable error, though at least 30% emittance reduction can be expected during acceleration. For injection, the maximum acceptable field error is 10%, and if safety factor of 2 is included, the field error requirement for injection is 5%. For the half sine wave option, the field error at the excitation can be neglected; only the residual field after one revolution needs to be considered. However, for the traveling wave option, the flattop region can fluctuate, and so the estimation of field error needs to take account of both the fluctuation of the flattop and the residual field. Table XVII summarizes the specifications.

For extraction, the requirements of kicker rise time can be also specified in a similar manner. For the half sine wave case the rise time should be shorter than 180 ns. For the traveling wave option the rise time should be shorter than 100 ns. A beam with emittance of 10π mm mrad injected with the field error discussed above is adiabatically damped to 6.3π mm mrad at the 70 MeV extraction energy. If the emittance of extracted beam is required to be less than 10π mm mrad, the acceptable field error at the flattop is

$$\frac{\Delta B}{B} = \frac{\sqrt{\beta\epsilon_{\text{ext}}} - \sqrt{\beta\epsilon_{\text{rev}}}}{X_{\text{septum}}} = \frac{\sqrt{1 \times 10} - \sqrt{1 \times 6.4}}{30} = 0.02.$$

TABLE XVII.   Specifications of injection kicker pulse.

Parameter	Unit	Value
Injection emittance	mm mrad	10π (unnormalized)
β_ν at injection	m	1
Orbit separation	mm	30
Fall time	ns	250 (traveling wave)
	ns	430 (half sine wave)
Acceptable field error	$\Delta B/B$	0.1 (without safety margin)
		0.05 (with safety margin: 2)

TABLE XVIII.   Specifications of extraction kicker pulse.

Extraction emittance	mm mrad	10π (unnormalized)
β_v at extraction	m	1
Orbit separation	mm	30
Rise time	ns	100 (traveling wave)
	ns	180 (half sine wave)
Acceptable total field error	$\Delta B/B$	0.02

The tolerance on the field of the extraction kicker is more severe than that of the injection kicker, since at injection, the beam emittance is small and adiabatic damping can be expected. For extraction, these are not expected and field error is directly converted into the final beam size. These requirements are summarized in Table XVIII.

2. Kicker design

The following equations were used in the analytical estimation of the kicker specifications:

$$L = (\mu_0 w l)/g \qquad \text{kicker inductance;} \qquad (13)$$

$$V = 2L(\Delta I/\Delta t) \qquad \text{voltage at kicker;} \qquad (14)$$

$$B = \mu_0 I/g \qquad \text{generated field strength;} \qquad (15)$$

$$\Delta x = \sqrt{\beta_{\text{kicker}}\beta_{\text{septum}}}\sin(\Delta\phi)\Delta x'$$
$$\text{orbit separation at septum,} \qquad (16)$$

where $\Delta I/\Delta t$ is the rate of change of the current, w, l, and g are the kicker width, length, and gap height, β_{kicker} and β_{septum} are the beta functions at the kicker and septum, $\Delta\phi$ is phase advance between kicker and septum, and $\Delta x'$ is kick angle. In Eq. (13) the influence of edge region is neglected, so inductance tends to be larger in the actual system. In Eq. (14) the pulse shape is assumed to be a traveling wave. In the case of a half sine wave kicker, the required voltage halves. The geometrical constraints for the kicker magnet are summarized in Table XIX.

Under the geometrical constraints and the requirements of extraction, the kicker aperture is 26 (V) × 185 (H) mm². With these apertures, the kicker specifications are estimated using Eqs. (13)–(16) (see Table XX). In this estimate, a single kicker per straight section is assumed

TABLE XIX.   Geometrical constraint of kicker design; "margin" means the space outside the beam excursion with the beam size of 10π mm mrad (unnormalized).

Thickness of septum conductor	mm	10
Margin at septum	mm	10
Margin of horizontal aperture	mm	10
Margin of vertical aperture	mm	10
Kicker length	mm	1000

TABLE XX.   Kicker specifications in PAMELA for vertical extraction (full coverage).

Parameter	Unit	
Orbit separation	mm	26 @ 250 MeV
Kicker inductance	μH	0.2
Magnetic field	T	0.06
Voltage	kV	30
Peak current	A	8200

and the pulse shape is assumed to be traveling wave. If the kicker is subdivided, the inductance per kicker and the power supply voltage halve.

Vertical extraction requires a large gap/width ratio magnet. In such a magnet, the inductance is difficult to estimate; the fringe field region is expected to deteriorate the field quality and increase the inductance considerably. The analytical estimates may be quite uncertain, and further studies using finite element analysis (and if possible hardware test) is needed. A tracking study was performed with ZGOUBI using an analytical field model for the kicker. Since the tune drift is quite small, a multiple kicker system with phase adjustment is not required. The behavior of the kicked beam with one kicker was investigated for horizontal and vertical extraction.

3. Finite element analysis

A dipole field of 0.06 T m is required to extract protons vertically at a maximum energy of 250 MeV. The kicker magnet is designed such that it can be used for both the proton and carbon rings. The extraction kicker of the carbon ring requires a 3 times stronger field (about 0.18 T m). The initial pulse length was specified as 250 ns, which is equivalent to a frequency of 2 MHz. The yoke is made of CMD5005 from Ceramic Magnets [41]; an alternative is the ferrite 8C11 from Ferroxcube [34]. Both ferrites should have a minimum permeability of 1000 at 2 MHz. The main purpose of the ferrite is to confine the magnetic flux; adding ferrite contributes to about 30% to the magnetic field. For the initial analysis a 2D finite element analysis (FEA) simulation is used. The yoke thickness is adjusted so that the magnetization is less than 300 mT, above which the ferrite would saturate. The magnetic energy is estimated to be 17 J/m; for a 1 m long kicker this is 17 J. A total current of just under 10 kA is required to generate the field for the proton case; for carbon this increases to about 30 kA. Assuming that the kicker is made of a single turn of wire, the inductance of the kicker is evaluated to be 0.34 μH. The field quality was evaluated using OPERA 3D, see Fig. 35 which shows the 3D model and the integrated horizontal field along the kicker.

4. Kicker magnet options

It is common practice to simplify a kicker and pulse forming network (PFN) setup by focusing on a fast rise or
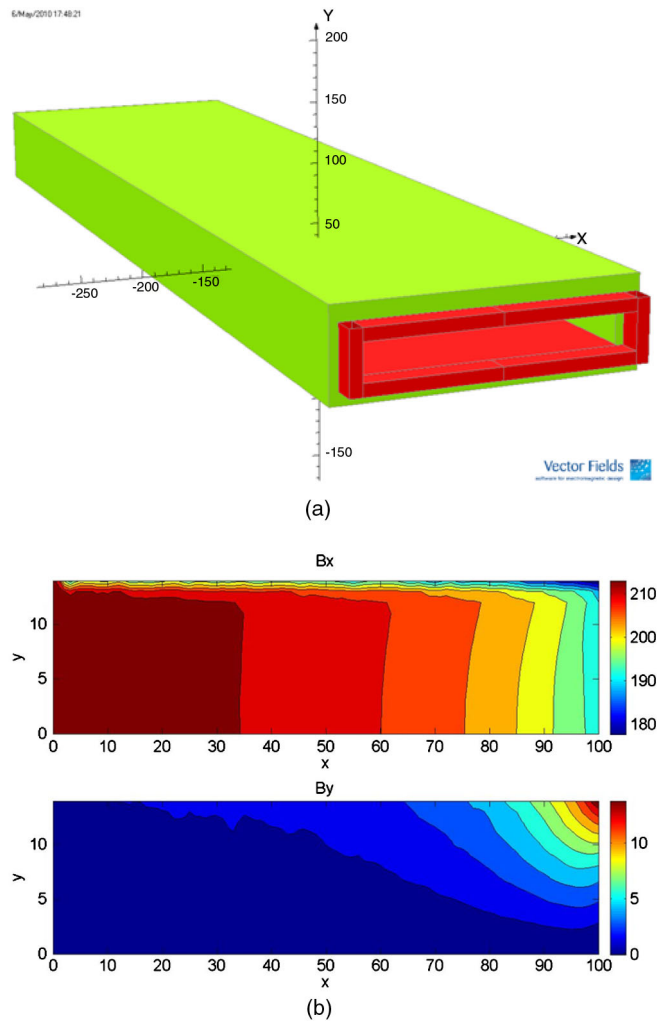
(a)

(b)

FIG. 35.   (a) 3D kicker model in OPERA and (b) integrated horizontal and vertical magnetic field in the kicker.

fall time. For an extraction kicker only the rise time is important, whereas for an injection kicker the fall time is crucial. For PAMELA it was decided to develop kicker systems which in general satisfy rise and fall times at the same time to minimize the development effort. The extraction kicker of the proton ring is therefore suitable as an injection kicker for the carbon ring. The same system can be used as an injection kicker for the proton ring at reduced voltage. The most demanding kicker is the extraction kicker for the carbon ring. The effort focused therefore on the extraction kickers of the proton and carbon ring.

In general, kicker magnets represent a lumped inductance, which leads to reflections when used in a PFN. Various approaches to this problem can be found in the literature. PAMELA employs two concepts shown schematically in Fig. 36. The proton lattice employs a double-bridged T-network [42] in which the lumped inductance of the kicker magnet appears to the PFN as a component with the correct impedance. The obvious advantage of this approach is that the kicker construction itself is
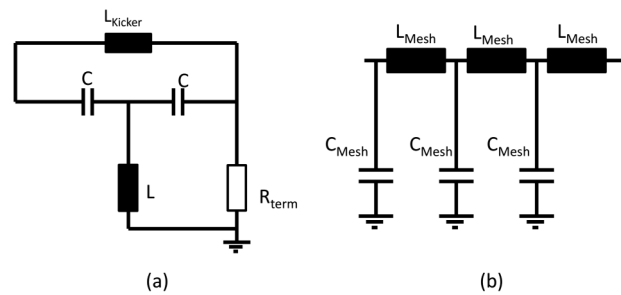

FIG. 36.   (a) Double-bridged T-network and (b) traveling wave kicker. For the double-bridged T-network the required capacitance C can be calculated from the kicker inductance and the termination resistance R: $C = L_{mag}/(2R_{term}^2)$. The required inductance can be calculated from $L = L_{mag}/4$.

simplified—no special preparation is necessary, an advantage at high voltages. The carbon lattice employs a traveling wave kicker, where the kicker is subdivided and capacitance is added to each section to achieve the required impedance. In practice this can be done by connecting SrTi capacitors to each section [43]. The capacitors can be either in the vacuum chamber or outside. Each section of the kicker magnet requires about 17.5 nF added capacitance to achieve a 1 Ω impedance (the inductance per section is 17.5 nH).

The ISIS fast extraction kicker is comparable in terms of peak current, rise/fall times, and pulse length to the extraction kicker of the PAMELA proton ring. The ISIS kicker system was therefore taken as a model and modified to suit the requirements. Its specifications are shown in Table XXI; it is powered by a PFN of lumped components, with a peak voltage of 36–60 kV at a current of 5000–8000 A and a rise time of around 100 ns.

The main difference for the PAMELA PFN system is the repetition rate, which for ISIS is 50 Hz while for PAMELA it is up to 1 kHz, which is more challenging for the

TABLE XXI.   ISIS fast extraction kicker specifications.

Parameters	Unit	value
Number of power supply systems		6
Number of magnets		3
PFN voltage	kV	36 (60 max)
Current	A	5000 (8000 max)
Current rise time	ns	80—120
Field rise time	ns	<210
Gap	mm	181
Pole width	mm	147
Magnet length	m	0.7
Bending angle	mrad	5.23
Cable impedance	Ω	6.25
PFN impedance	Ω	3.75×2
Magnet inductance	mH	$0.39 + 0.39$
Magnetic field	T	0.0365

TABLE XXII.   Specification of the PAMELA PFNs.

		Proton	Carbon
Rise time	ns	100	100
Flattop	ns	100	100
Fall time	ns	100	100
Rep rate	kHz	1	1
Current	kA	10	30
Voltage	kV	60	60
Inductance kicker	μH	0.1–0.2	0.1–0.2
Length	m	2×0.5	2×0.5
Sections		Lumped	10
Impedance	Ω	3	3/1
C_{Mesh}	nF	11.67	11.67
L_{Mesh}	nH	105	105

individual components and the cooling. An additional challenge for the carbon system is the required peak current, which is 30 kA instead of 10 kA. A further difference is that the ISIS system is not terminated, which doubles the voltage across the kicker magnet, leading to undesirable reflections. The specifications for the PFNs for the PAMELA proton and carbon case are summarized in Table XXII. To keep all PFNs similar, the proton PFN

has the same impedance as the carbon PFN, allowing the same components to be used.

Both PFNs operate at voltages up to 60 kV. The impedance for the proton PFN is 3 Ω, which leads to a peak current of about 10 kA. To achieve the necessary 30 kA for the carbon kicker, three of these PFNs are connected in parallel and fired into a 1 Ω load. This is shown schematically in Fig. 37(b).

To achieve the necessary rise and fall times the inductance per PFN is restricted to a maximum of 0.2 μH. The kicker inductance is about twice this, which means each kicker needs to be subdivided into two. Therefore, two PFNs are necessary for the proton kicker and six PFNs for the carbon kicker. The resulting pulse shapes calculated using SPICE are shown in Fig. 38. For the carbon lattice the current has been averaged over all ten sections of the kicker magnet. As shown, both kickers meet the rise time requirements of 100 ns. The carbon kicker has a longer fall time, which is acceptable as the kicker is used for extraction only.
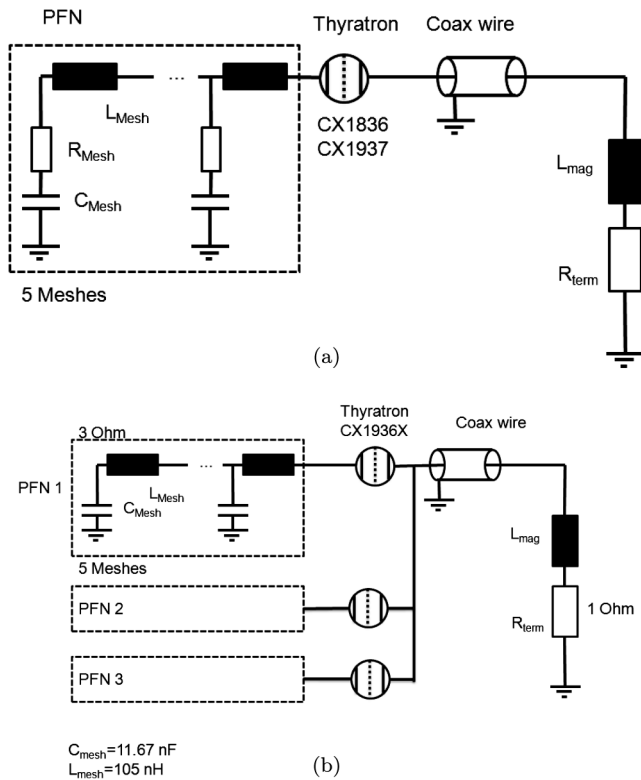

FIG. 37.   Schematic of the PFN for (a) protons and (b) carbon. The thyratrons have been selected after extensive discussions with e2V. The kicker magnet is shown schematically as a resistance and inductance.
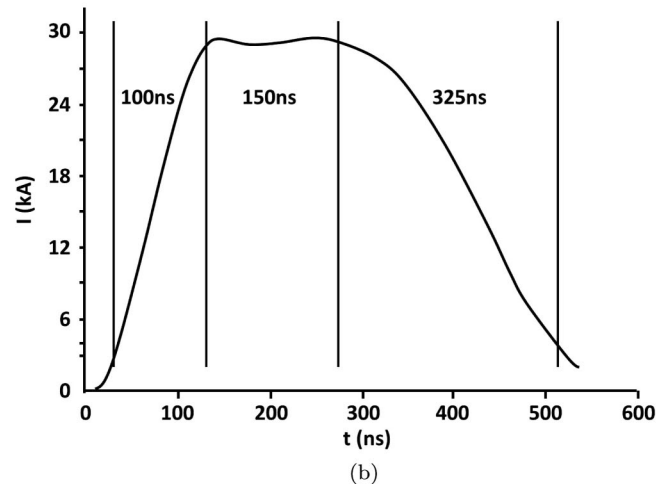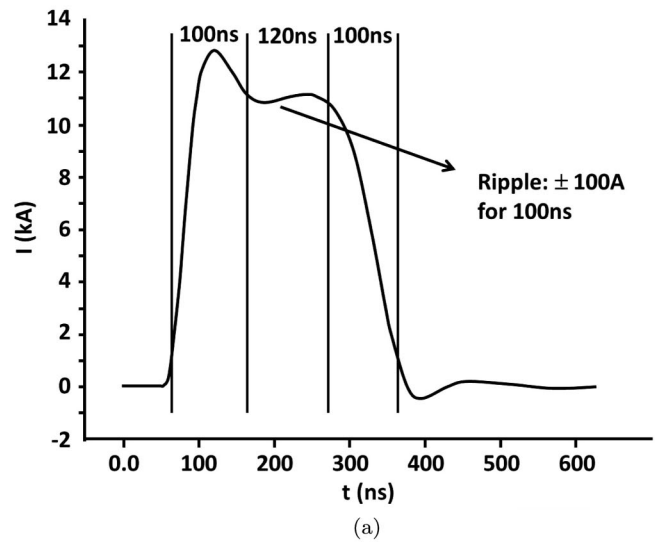

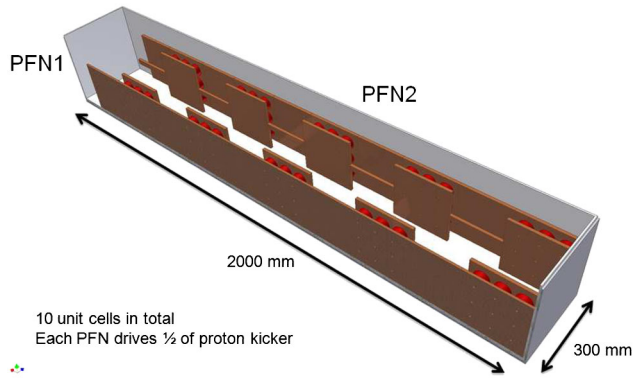FIG. 38.   Pulse shapes of the (a) proton and (b) carbon kicker.

FIG. 39.   A complete PFN assembly for a kicker for the proton ring; the box houses two PFNs.

Various manufacturers of capacitors have been approached and suitable components are, for example, a General Atomics PM/PD capacitor [44]. The GA capacitor can meet the lifetime requirement of 3×10^{11} pulses [46]. A second 29 option is a ceramic capacitor from TDK (FHV-11AN) which has a capacitance of 1300 pF [45]; nine of these in parallel match the required capacitance of 11.67 nF. This assumes that the TDK ceramic capacitor is used; a design based on the GA capacitor would look similar. Nine capacitors are connected between two copper plates. The mesh inductance uses a suitably dimensioned copper bar. The complete assembly housing the two PFNs for the proton kicker is shown in Fig. 39. Subject to sufficient cooling the entire assembly would occupy about 2×0.3 m^2 of floor space. The carbon assembly would consist of three of these boxes.

The double-bridged T-network approach was tested with a simple trial circuit, which is shown in Fig. 40. The circuit operates at 50 V, sufficient to verify the concept, and was based on a 2 Ω proton PFN approach, but similar results can be expected for the now favored 3 Ω design. The voltage across the magnet inductance is shown in Fig. 41, which resembles the expected result. The discrepancy results from the mesh inductances, which are hand wound and therefore prone to substantial variation.
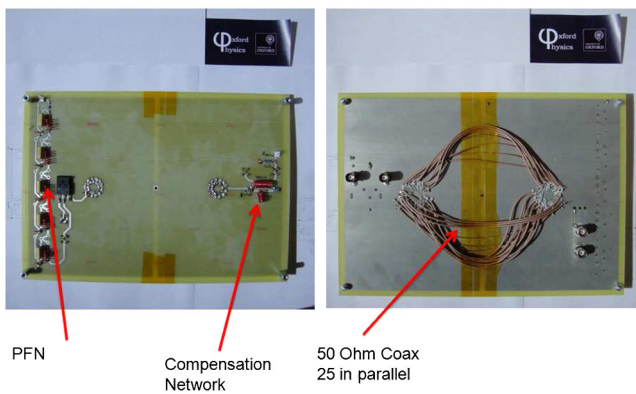

FIG. 40.   PFN test circuit, courtesy of Johan Fopma (Oxford).
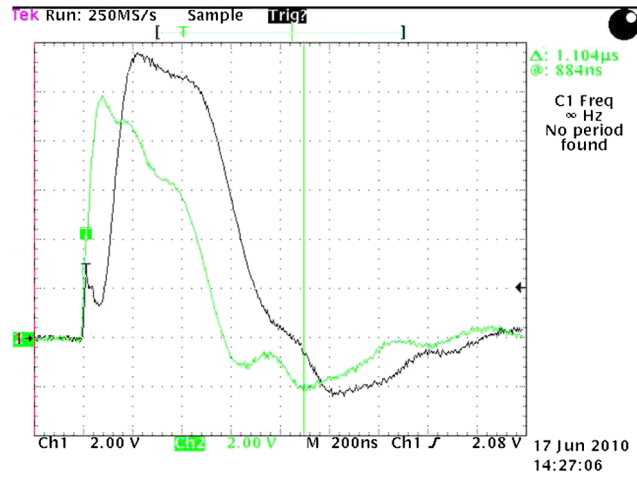

FIG. 41.   PFN test circuit—voltage across magnet.

B. Septum specifications

After the septum, the beam is directed out of the ring so that the estimate for septum magnet is a simple geometrical calculation, summarized in Table XXIII. Using the parameters of the proton ring and the assumption that the drift length and magnet dimension of the carbon ring are similar to those of the proton ring, the field requirements of septum are estimated for both rings, given in Table XXIV. The required field of the proton ring is achievable using a normal-conducting septum (pulsed). For the carbon ring, a superconducting septum is required owing to the high 4 T field.

PAMELA requires variable energy extraction to treat tumors at different depths in human tissue. This implies that the kicker field needs to be adjusted for each extraction energy, which can easily be done by charging the PFN to a different voltage level. However, more challenging is the septum, which needs to provide a magnetic field of up to 4 T in a large bore. The combination of field and bore rule out a normal-conducting solution, and the power requirements even for a pulsed septum would be enormous. A field of 4 T is certainly well within the possibilities of commercially available superconductors; one problem however is the large stored energy, which leads to a large inductance. Changing the field of the septum at kHz rates would require a very high voltage power supply. One solution is to sweep the septum at a lower rate, either by reducing the repetition rate or by restricting the treatment modalities—neither of which is very attractive, as fast acceleration is one of the main features of an FFAG.

TABLE XXIII.   Geometrical constraints of the septum magnet.

Parameter	Unit	Value
Available space in long drift	m	1.2
Length of septum	m	1.0
Outer radius of magnet module 7	m	0.4

TABLE XXIV.   Field strength of extraction septum.

Parameter	Unit	Values Proton ring	Carbon ring
Energy	MeV/u	250	440
Septum field	T	1.6	4.0 T
Orbit separation	m	0.41	0.40

A conceptual design of a superconducting septum is described, which allows particles to be extracted at different energies without the need for sweeping the magnet. This is called a FFAG septum, where the horizontal magnetic field varies as a function of the horizontal position. As the particles in the FFAG have a different horizontal position depending on their energy, each particle receives the correct amount of bending, meaning all particles have the same bending radius. The extraction septum for the carbon ring is the most demanding. The same design is then in principle suitable for the proton ring when operating at a lower current.

Figure 42 shows the geometry of the septum; in green is the iron yoke, which is necessary to confine the magnetic flux. The circulating beam is shielded from stray fields by a separate soft-iron shield. The shield has been designed
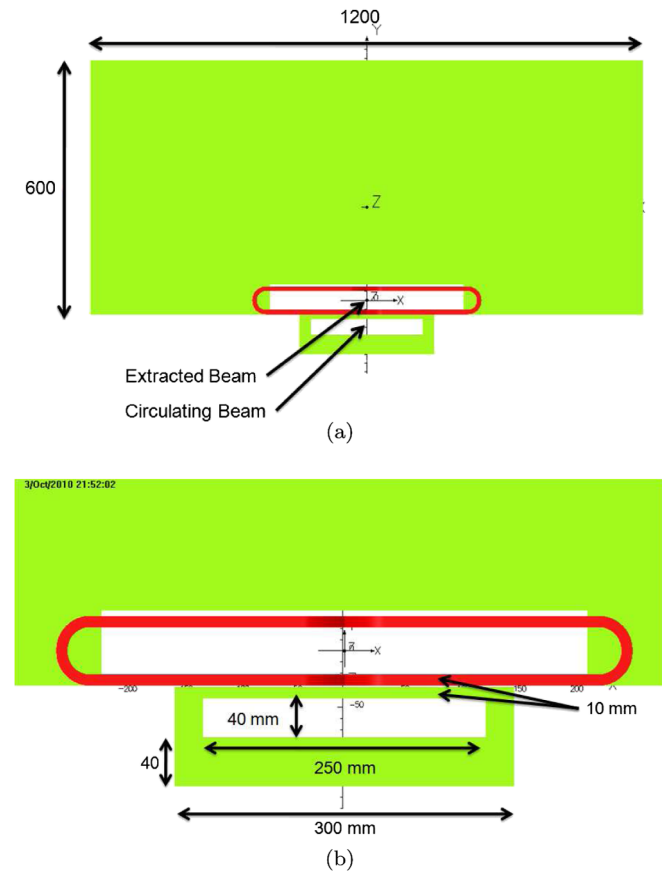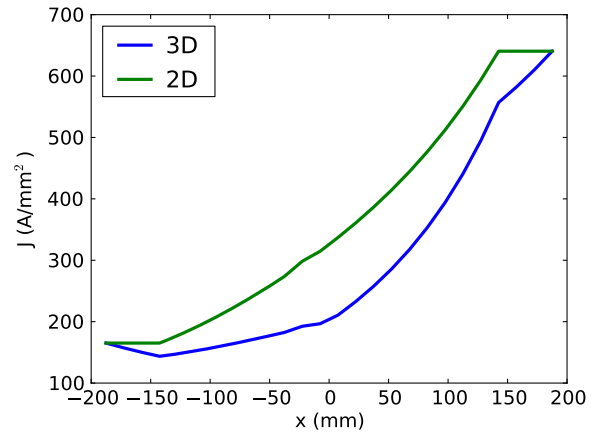

FIG. 43.   Current density in the bedstead coils as a function of the horizontal position. Shown are the theoretically required current density for a 2D case and the final current density in the model, which takes into account the different lengths of the bedstead magnets and nonlinearities of the iron yoke.

using FEA (OPERA 3D). The septum aperture for the circulating beam is 250×40 mm^2. The length of the iron yoke is 600 mm. The two bedstead coils are shown in red, which are the positive and negative current sheets necessary to generate the desired horizontal magnetic field. Each bedstead coil consists of 13 individual coils, which all have different current densities and different lengths. The horizontal magnetic field of the septum should follow roughly the scaling law. To achieve this, the current density in each bedstead coil is carefully adjusted; the resulting net current density as a function of the horizontal position is shown in Fig. 43, obtained in an iterative process using OPERA 3D as the response in field is nonlinear.

The current density in each coil was varied until the desired field was matched within 1%. The resulting horizontal field (integrated) is shown in Fig. 44 in comparison

FIG. 42.   Front views of the extraction septum for the carbon ring (a) whole septum (b) detail.
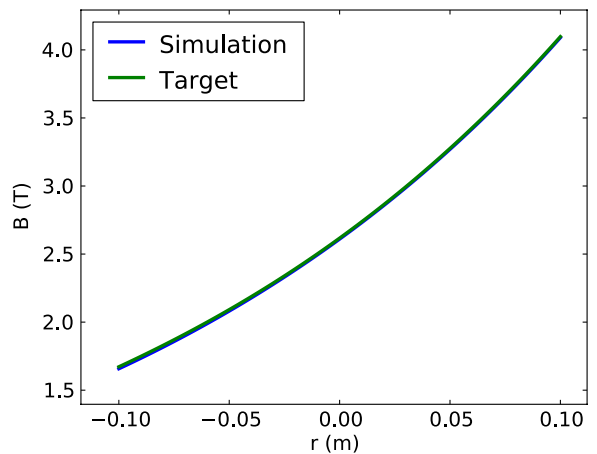

FIG. 44.   Horizontal magnetic field in the septum as a function of the horizontal position. The real magnetic field is averaged over various vertical positions within the septum bore.

to the targeted field; Fig. 45 shows the integrated horizontal and vertical magnetic field in the septum bore as a function of the horizontal and vertical position. The figures illustrate that a good match to the desired horizontal field can be obtained; it should be noted that the created field is not a pure dipole field, but vertical field components are present as well. Depending on the position, the vertical field can be as high as 0.3 T.

To investigate the feasibility of this design we assume a superconductor with a Cu:Sc ratio of about 1:1. The peak magnetic field on the wire is about 6.7 T. Because of the Cu:Sc ratio the critical current density in the superconductor itself will be around 1200 A/mm^2. One option is to use Nb$_3$Sn, which has a critical current density of 4500 A/mm^2 at 4.2 K and 6.7 T. This value considers that the current density in a commercially available conductor may be somewhat degraded in comparison to lit-
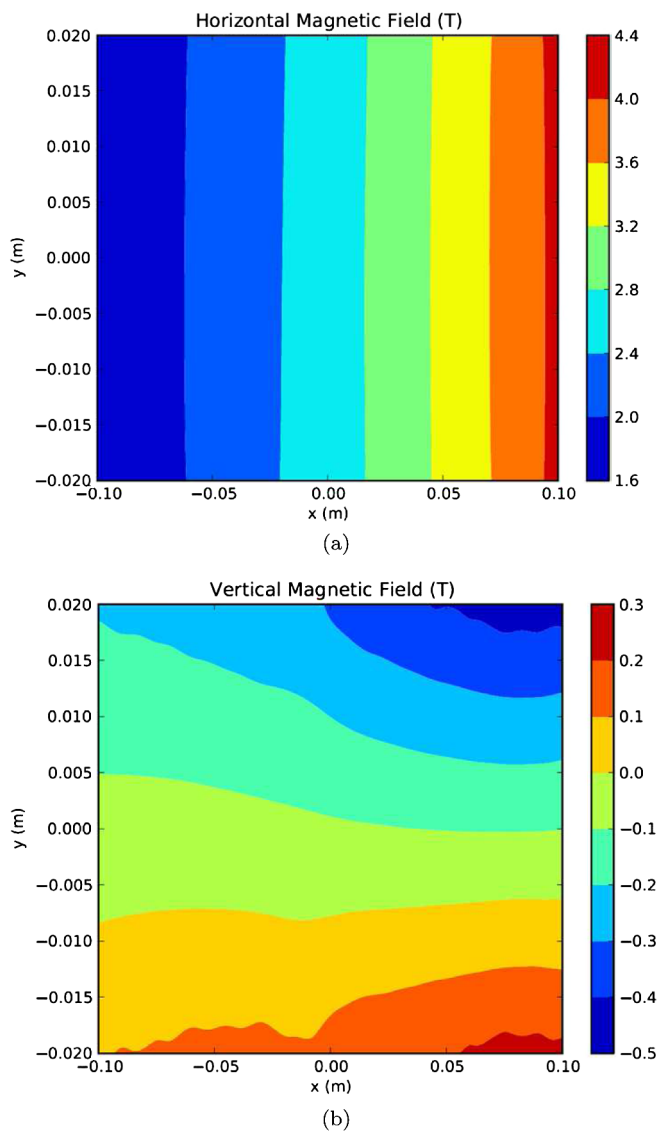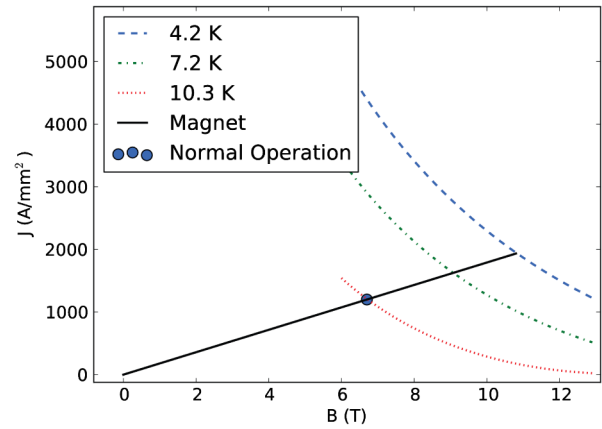

FIG. 46. Load line of the FFAG septum.

erature values. The data are taken from [47]. According to literature values, the temperature margin of the septum should be about 6 K. Nb$_3$Sn at 6.7 T at 10 K has a critical current density of 1400 A/mm^2, which is slightly higher than what is necessary for the septum (1200 A/mm^2). Figure 46 shows the load line for the septum.

One potential issue with a high-field septum like this is the stray field, illustrated in Fig. 47. The figure shows the septum from underneath; the vertical magnetic field is plotted over a patch 1 mm below the bedstead coils. The area covered by the iron yoke is denoted by the box in light blue. There is a large amount of stray magnetic field present, which arises from two sources: the coils themselves and flux leaking out of the bore of the septum; this is particularly problematic at the coil ends. To compensate, the beam pipe has been encased in a magnetic shield, the geometry of which has been optimized using FEA. The

FIG. 45. Integrated horizontal (a) and vertical (b) magnetic field in the septum bore as a function of the position.
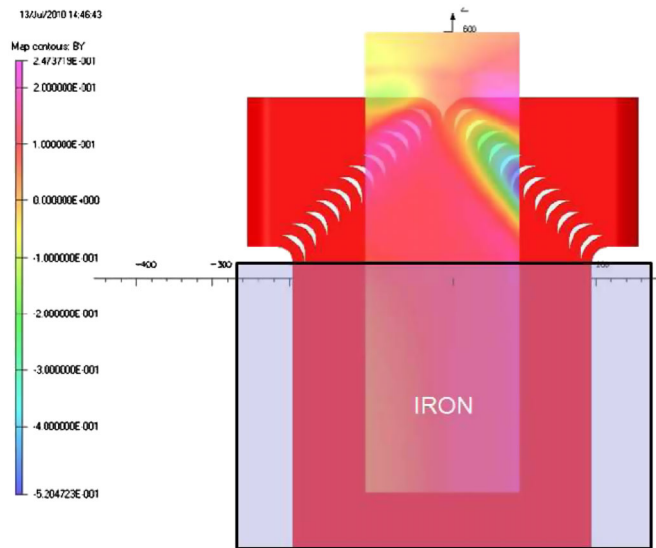

FIG. 47. Vertical stray field experienced by the circulating particles. The septum is shown from underneath, the light blue area indicates the part which is covered by the iron yoke.
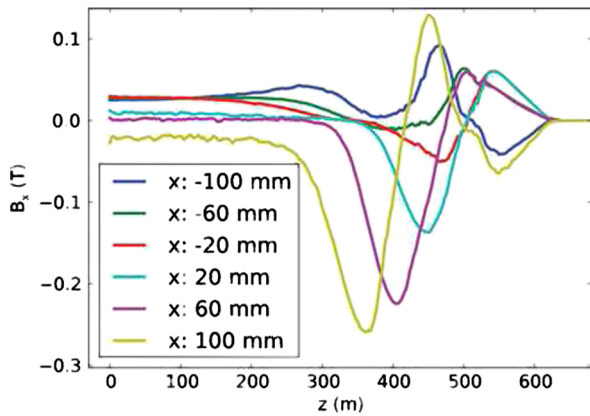
FIG. 48. Stray horizontal magnetic field at a vertical position of -43 mm. The field is shown for a horizontal position from -100 to 100 mm in 40 mm steps [56].

horizontal magnetic field experienced by the circulating beam is shown in Fig. 48, in which the horizontal magnetic field is plotted at six horizontal positions across the aperture at a vertical position of -43 mm (which is on the upper side of the iron shield, see Fig. 42). The maximum integrated field level of 0.04 T m has been found to be acceptable for the operation of PAMELA.

IX. BEAM TRANSPORT AND GANTRY

A typical particle therapy facility has multiple treatment rooms, to which beam is delivered from the accelerator. The beam line downstream of the extraction system is known as the "beam delivery system." The basic requirement of the beam delivery system is to transport the beam from accelerator to the treatment system without distortion. To achieve this, the main functions for active beam scanning irradiation are: (i) matching optics of the accelerator and the treatment system by including orbit error correction in the transport line and, for a gantry, matching with rotating optics; in addition, active beam scanning requires precise beam position control; (ii) transporting the proton beam energies from 70 to 250 MeV which, in a single treatment, could vary over a maximum range of about 40 MeV with an acceptably short latency; (iii) shaping the beam for active scanning in accordance with the prescribed treatment plan, typically from 4 to 10 mm (FWHM); and (iv) switching the beam between treatment rooms and into a beam dump.

PAMELA incorporates variable energy extraction in a fixed field accelerator, using vertical beam extraction. Since the beam is extracted vertically, the horizontal orbit excursion in the ring is conserved after extraction. In addition, since PAMELA employs fast extraction, in principle the extracted beam energy can change bunch by bunch. The transport system must handle a large momentum range with substantial orbit excursion, 70 to 250 MeV (see Sec. II) and the orbit excursion corresponding to the energy range is about 11 cm (see Sec. IV).

The requirements of large momentum acceptance and wide orbit excursion are the major challenges in the design of the beam transport line. In order to achieve this, a FFAG beam transport line (FFAG-BTL) is proposed [48]. Note that, so far, only a proton transport line has been studied; a carbon transport line may be designed using the same principles.

FFAG accelerators are characterized by a scaling law in which the field strength increases with radius. A straight FFAG may seem a counterintuitive idea. However, since a straight line can be considered as a curve with an infinite radius, the scaling law may be recast into a form that approximates a straight FFAG by defining the radius of its reference orbit to be much larger than the orbit excursion. An FFAG magnet in a circular machine obeys the scaling law given by Eq. (1). In a beam transport line, on the other hand, there is no machine center. It has been shown that a scaling magnet in a beam transport line has an exponential field profile [49], of the form in Eq. (17):

$$B_y(x, z) = B_{y0} \exp[(n/\rho)x]F(z), \qquad (17)$$

where (x, y, z) are respectively the horizontal, vertical, and longitudinal coordinates, ρ is the radius of curvature, $n = (\rho/B_y)(dB_y/dx)$, and $F(z)$ is a periodic function of the longitudinal coordinate z. For clarity n/ρ is substituted for k/x_0. Noting that

$$\lim_{x_0 -> \infty} [(x_0 + x)/x_0]^k = \exp[(n/\rho)x], \qquad (18)$$

then by analogy with the magnet for a scaling FFAG, but in Cartesian geometry, a FFAG-BTL magnet may be defined with the following field profile:

$$B_y(y, z) = B_{y0}[(x + x_0)/x_0]^k F(z), \qquad (19)$$

where x is the horizontal distance from x_0, B_{y0} is the vertical field at x_0. In the limit of large r_0 it can be seen from Eq. (1) that the arc of a scaling FFAG will tend towards a straight line and so it may be supposed that Eq. (19) is a reasonable assumption in the case of large x_0. Equation (19) may be expanded as a Taylor series:

$$B_y(x, z) = B_{y0}\left(1 + \sum_{n=1} \frac{1}{n!} \frac{k(k-1)\ldots(k-n+1)}{x_0^n}\right)F(z).$$
$$(20)$$

It follows that the quadrupole term is proportional to k/x_0 and so to keep the lowest order focusing strength unchanged, k should be increased by the same factor as x_0. In the following, the ratio k/x_0 is called the *normalized field index*, and is used rather than separately referring to k and x_0. Notice that the magnet has a rectangular shape and the constant field lines are straight along the BTL. As in the main ring, a nonscaling FFAG-BTL magnet may be created by truncating the Taylor expansion at some multipole term, thus simplifying the magnet design. The FFAG-BTL is

described in more detail in [48]. Note that an experimental straight FFAG, using magnets with exponential field profiles, is under construction at KURRI [50].

The length of transport line considered is 30 m, the distance from the first to the last treatment room. To make the transport line sparse while keeping a periodicity that fits the distance between treatment rooms, a cell length of 5 m was chosen. The magnets are arranged in a DFFD configuration where F is a horizontally focusing magnet and D is defocusing. In this configuration, the orbit at the entrance and exit is perpendicular to the magnet faces. The magnets are 20 cm long with a 20 cm short drift space between each magnet followed by a long drift of 3.6 m. The full set of parameters of the cell is listed in Table XXV— the choice of cell focusing structure, normalized field index and fields is determined by an optimization process described below. In order to simplify the magnet design, multipoles up to decapole are used [Eq. (20)]. It is found that this is sufficient to ensure a near constant cell tune over the momentum range. As in a scaling FFAG, the cell tune may be adjusted by varying the ratio k/x_0 or the ratio of the field strength in the F and D magnets.

To determine the optimal normalized field index k/x_0, the magnet strengths (i.e. the D/F ratio) and the lattice structure (FDDF or DFFD), several factors are taken into consideration. These are the acceptances over the 30 m length of the transport line, the orbit excursion, the required magnet aperture and field and the dispersion in the center of the long drift where switching into the treatment rooms is located. Optimizing for each of these factors simultaneously may require compromise.

The minimal required acceptance is given by the emittance of the extracted beam—the normalized value is about 10π mm mrad. Configurations with an orbit excursion exceeding 20 cm were rejected to allow a realistic magnet design, while to facilitate matching from the main ring, a configuration was chosen so that the difference between the highest and lowest closed orbits at the center of the long drift is close to 15 cm, although matching from the main ring has not been demonstrated and needs further study.

Because the transport carries the beam over a relatively short distance, a definition of acceptance that relies on loss of particles would not be particularly useful. More useful is a measure of the distortion of the position and shape of the horizontal and vertical phase space ellipses. This definition has been chosen making use of the "smear" of a phase space ellipse of particles, defined as the rms deviation of the individual particle emittances from the average initial emittance. i.e. it is a measure of the distortion of the beam. It may be written as follows:

$$\text{smear} = \sqrt{\langle(\epsilon_i - \langle\epsilon_i^{ini}\rangle)^2\rangle/\langle\epsilon_i^{ini}\rangle}, \qquad (21)$$

where ϵ_i is the individual particle emittance given by the particle amplitude as follows:

$$\epsilon_i = \beta x_i'^2 + 2\alpha x_i x_i' + \gamma x_i^2, \qquad (22)$$

where y and α, β, γ refer respectively to the coordinate and optical parameters in either transverse plane and ϵ_i^{ini} is ϵ_i at the entrance of the channel, illustrated in Fig. 49.

The acceptable level of smear should be established by the tolerance of the downstream gantries and by the clinical requirements. For this study it is assumed that a distortion of 10% is acceptable—at this level the optical distortion is minimal. The acceptance, then, is defined as the emittance which distorts the beam (in either plane) to such an extent that the smear is 0.1 over the length of lattice (see [51] for a more complete description of how the acceptance has been calculated).
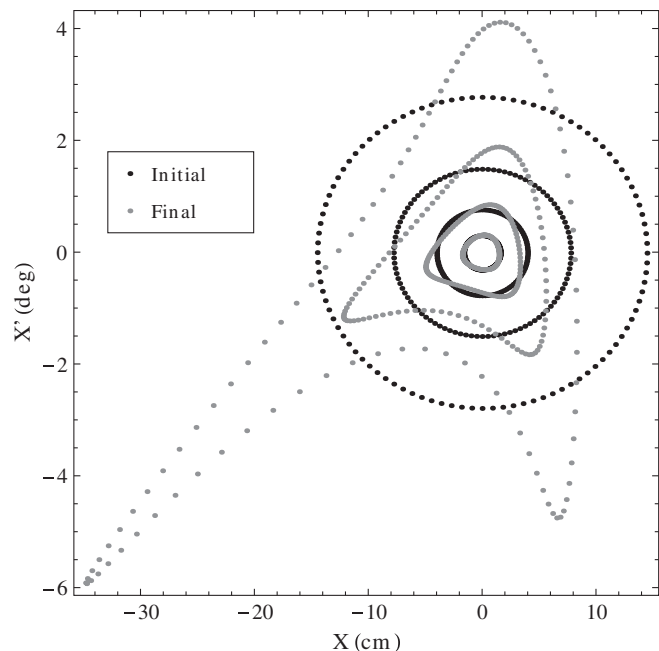

FIG. 49. Phase space ellipses of four emittances that result in smears of 0.1, 0.25, 0.5, and 1. The black dots represent the particles at the start of the lattice while the grey dots represent the same particles at the end. Increasingly large initial emittances are used simply for clarity in the figure.

TABLE XXV. Parameters of DFFD cell for the FFAG-BTL.

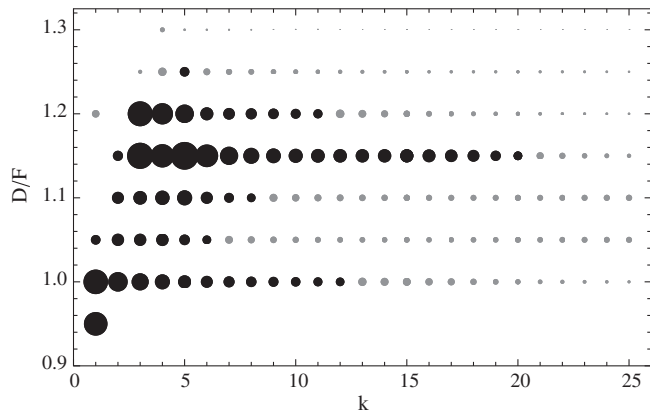| Focusing		DFFD
Magnet length	m	0.2
Short drift length	m	0.2
Long drift length	m	3.6
Cell length	m	5.0
Field index k/x_0	m^{-1}	11 (Normalized)
Reference momentum	MeV/c	549
Momentum range	MeV/c	369 to 729
B_{y0} at F	T	0.36
B_{y0} at D	T	-0.43
Enge coefficients		0.146, 2.267, -0.640, 1.156
Magnet width	m	0.15

FIG. 50. The acceptances for 30 m of transport line using cells with nonscaling magnets in a DFFD configuration. The size of the dots are proportional to the square root of the acceptance. Black dots represent acceptances >10 mm mrad and grey dots represent lower acceptances. For scale: the largest acceptance (at $k/x_0 = 5$ and D/F = 1.15) is 101.75π mm mrad and the smallest (at $k/x_0 = 20$ and D/F = 1.3) is 0.03π mm mrad.

Closed orbits were found for the lowest, an intermediate, and the highest momenta (369, 549, and 729 MeV/c, respectively) and a set of particles were then tracked with increasing initial emittances until the smear exceeded the 0.1 limit. The exercise was repeated with decreasing emittance steps until the smear limit was approached with adequate precision. The lowest acceptance was taken to be representative of the working point, although little variation with momentum was observed.

An initial study was conducted in which the value of the normalized field index k/x_0 was varied in the range 1 to 25 and the D/F field ratio was varied from 0.95 to 1.3. Note, nonscaling magnets are used and the field index refers to the value from the Taylor expansion [Eq. (20)]. The results for the case of the DFFD and FDDF lattices are shown in Figs. 50 and 51, respectively. It is clear from these results that there are working points with sufficient acceptance. It is also apparent that there more points with high acceptance in the DFFD configuration and for this reason this lattice configuration is preferred.

The dependence of the dispersion in the center of the long drift on the field index is shown in Fig. 52. There is a conflict between using higher k values to reduce the dispersion at the center of the long drift and using lower k values to increase the acceptance, but from inspection it seems that there are good compromises available around $k/x_0 = 12$, D/F ratio = 1.15 with a DFFD cell configuration. A more detailed study was carried out in this region, the results are shown in Fig. 53. The results indicate a promising working point at $k/x_0 = 11$, D/F ratio = 1.17, where the acceptance is 122π mm mrad. Figures 54–56 show the equilibrium orbits, beta functions, and fields along equilibrium orbits
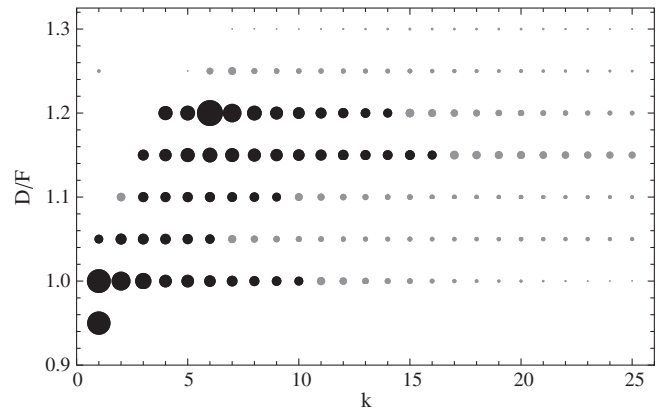

FIG. 51. The acceptances for 30 m of transport line using cells with nonscaling magnets in a FDDF configuration. See Fig. 50 for description of dot size and color.
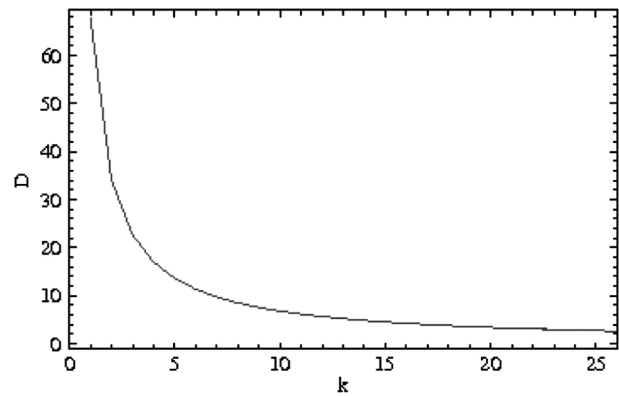

FIG. 52. The dependence of the dispersion in the center of the long drift of a transport cell on the field index k/x_0.
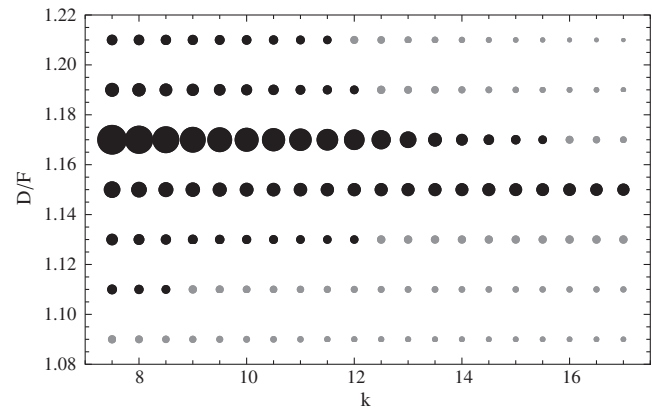

FIG. 53. The acceptances for 30 m of transport line using cells with nonscaling magnets in a DFFD configuration, k/x_0 close to 12 and D/F close to 1.15. For scale, the largest dot at $k/x_0 = 7.5$ and D/F = 1.17 represents an acceptance of 122.03π mm mrad. See Fig. 50 for description of dot size and color.
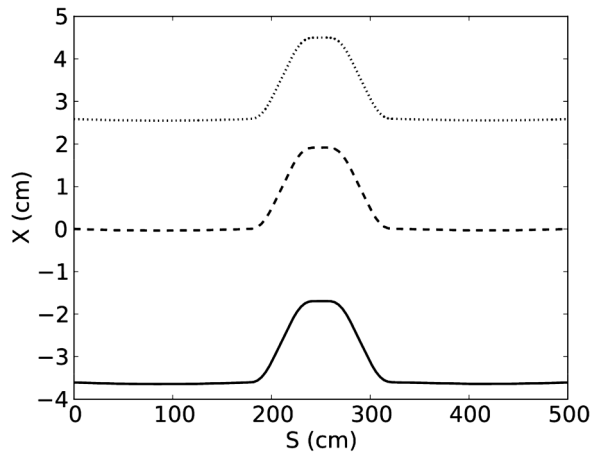
FIG. 54. Equilibrium orbits at 369, 549, and 729 MeV/c through cell with $k/x_0 = 11$ and a DF ratio of 1.17. In ascending order of momentum the orbits are shown as solid, dashed, and dotted lines.

through one cell at this working point. The largest smear is 0.064 in the horizontal phase space, well within the tolerance discussed above.

A. Gantries

Dose deposition with charged particle therapy has the important advantage of being efficient in sparing healthy tissue with the help of the Bragg peak. To maximize the advantage, it is desirable to set the beam direction so that an optimum dose field can be formed, a process known as "active scanning." Current technology uses a rotating gantry which allows the beam to be delivered from any direction in the vertical plane. In combination with the patient-table rotation, this makes it possible to irradiate the patient from any direction specified by clinical need. Gantries are widely used in conventional radiotherapy and are becoming common in newer proton therapy facilities
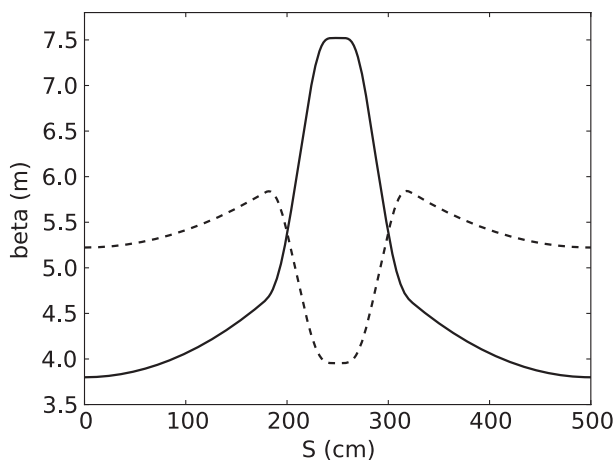

FIG. 55. Horizontal (solid) and vertical (dashed) beta functions through cell with $k/x_0 = 11$ and a DF ratio of 1.17.
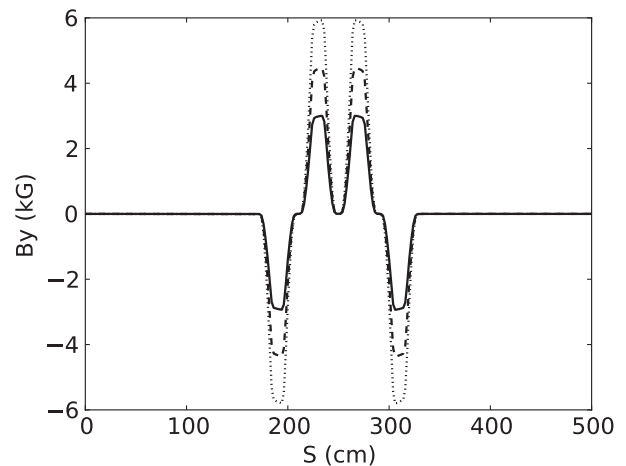

FIG. 56. Fields along the equilibrium orbits at 369, 549, and 729 MeV/c through cell with $k/x_0 = 11$ and a DF ratio of 1.17. In ascending order of momentum the orbits are shown as solid, dashed, and dotted lines.

[52]. On the other hand, there is only one gantry for carbon ions, although a few are in the design stage [53].

There are two main active scanning procedures—"raster scanning" and "spot scanning." In raster scanning, the beam is delivered continuously and the intensity modulation is carried out by changing the scanning speed of the beam. The advantage of raster scanning is its relative simplicity. It can easily be extended from the wobbler system of broad beam irradiation. On the other hand, due to the lack of a beam-off period, it has a limitation in irradiating complicated-shaped target volume. Spot scanning provides dose with a pulsed beam. Intensity modulation is achieved by varying the pulse intensity so that it matches the prescription at each target point. This scheme can create a beam-off period, and so can flexibly accommodate the shape of the target volume. The FFAG extracted beam naturally has a pulsed structure so that spot scanning is the natural choice. The beam requirements for spot scanning were discussed in Sec. II.

The high extraction rate at variable energy implies a gantry that also has fixed field magnets for the main beam transport—an FFAG gantry. A linear, nonscaling FFAG gantry concept has been proposed [54], but has a very dense doublet lattice structure. A novel nonlinear, nonscaling FFAG isocentric gantry has been studied, and a preliminary design for a proton gantry exists [55]. However, this work is still in a preliminary state, and will be the subject of a separate paper.

X. SUMMARY AND CONCLUSIONS

The conceptual design for PAMELA a combined proton and carbon ion therapy machine is presented using a non-scaling fixed field alternating gradient accelerator. The machine is capable of delivering high dose rates in spot

scanning mode, with kHz variable energy extraction. The design is a ''proof of principle'' that such a machine can meet the demanding clinical requirements. The design includes not only the central accelerators but also preliminary ideas for the ion sources, injection and extraction, beam transport and gantries, which are challenging because of the special features of FFAGs, if the advantages of the rapid energy variation and extraction are to be fully utilized.

While the conceptual design presented here meets the challenging specifications, it also involves advanced technologies, particularly in the magnets and rf. The next stage towards the construction of a prototype PAMELA accelerator is to develop preproduction prototypes of these principal components—the ion sources and injection beam transport system, the injection and extraction kickers and septum magnets, the main ring triplets and the rf cavities and power supplies. Many of these components are technologically challenging. Simulation has shown that they can be constructed within the known bounds of current technology. Nevertheless, there are residual risks that the component prototyping phase should address, as well as laying the foundations for subsequent industrialization of the production machine.

Future development would include extending the C^{6+} ion source to accelerate H_2^+, allowing in principle other light ions (especially $^4_2$He or $^6_3$Li) to be used, and exploring whether a combined proton and carbon ion ''racetrack'' configuration would provide substantial advantages, with a smaller footprint and lower cost.

Although charged particle therapy has been in clinical use now for more than 50 years, there are still significant accelerator challenges to be overcome before the technology is capable of delivering the required dose in an optimal way.

ACKNOWLEDGMENTS

[1] For a general review, see J. Schippers and A. Lomax, Acta Oncologica **50**, 838850 (2011).

[2] S. Peggs, T. Satogata, and J. Flanz, in *Proceedings of the 2007 Particle Accelerator Conference, Albuquerque, New Mexico* (IEEE, New York, 2007), pp. 115–119.

[3] T. Ohkawa, in Proceedings of the Annual Meeting of JPS (1953).

[4] K. Symon, D. Kerst, L. Jones, L. Laslett, and K. Terwilliger, Phys. Rev. **103**, 1837 (1956).

[5] A. Kolomensky and A. N. Lebedev, *Theory of Cyclic Accelerators* (North-Holland, Amsterdam, 1966).

[6] C. Johnstone, W. Wan, and A. Garren, in *Proceedings of the 18th Particle Accelerator Conference, New York, 1999*, edited by A. Luccio and W. MacKay (IEEE, New York, 1999), p. 3068.

[7] R. Barlow *et al.*, Nucl. Instrum. Methods Phys. Res., Sect. A **624**, 1 (2010).

[8] S. Machida *et al.*, Nat. Phys. **8**, 243 (2012).

[9] T. Yokoi, J. Cobb, K. Peach, and S. L. Sheehy, in *Proceedings of the 11th European Particle Accelerator Conference, Genoa, 2008* (EPS-AG, Genoa, Italy, 2008), pp. 3398–3400 [http://www.JACoW.org].

[10] S. L. Sheehy, D.Phil. thesis, University of Oxford, UK, 2010.

[11] S. Sheehy and D. Kelliher, Int. J. Mod. Phys. A **26**, 10 (2011).

[12] S. L. Sheehy, K. J. Peach, H. Witte, D. J. Kelliher, and S. Machida, Phys. Rev. ST Accel. Beams **13**, 040101 (2010).

[13] *Proton Therapy Physics*, edited by H. Paganetti (CRC Press, Boca Raton, FL, 2012).

[14] T. Kanai *et al.*, Med. Phys. **7**, 2871 (1980).

[15] The MAD-X home page: http://frs.home.cern.ch/frs/Xdoc/mad-X.html.

[16] C. Johnstone, W. Wan, and A. Garren, in *Proceedings of the 18th Particle Accelerator Conference, New York, 1999* (IEEE, New York, 1999), p. 3069 [http://www.JACoW.org].

[17] E. Keil and A. M. Sessler, Nucl. Instrum. Methods Phys. Res., Sect. A **538**, 159 (2005).

[18] D. Trbojevic, E. D. Courant, and M. Blaskiewicz, Phys. Rev. ST Accel. Beams **8**, 050101 (2005).

[19] R. Baartman, in Proceedings of FFAG 2004 (unpublished).

[20] S. Machida and D. J. Kelliher, Phys. Rev. ST Accel. Beams **10**, 114001 (2007).

[21] C. Johnstone and S. Koscielniak, in *Proceedings of the 10th European Particle Accelerator Conference, Edinburgh, Scotland, 2006* (EPS-AG, Edinburgh, Scotland, 2006), p. 2290 [http://www.JACoW.org].

[22] S. Machida, Phys. Rev. ST Accel. Beams **11**, 094003 (2008).

[23] S. Machida, Phys. Rev. Lett. **103**, 164801 (2009).

[24] F. Méot, Nucl. Instrum. Methods Phys. Res., Sect. A **427**, 353 (1999).

[25] S. Machida, ICFA Beam Dyn. Newslett. **43**, 54 (2007).

[26] H. Witte, T. Yokoi, S. Sheehy, K. Peach, S. Pattalwar, T. Jones, J. Strachan, and N. Bliss, IEEE Trans. Appl. Supercond. **22**, 4100110 (2012).

[27] D. Meyer and R. Flasck, Nucl. Instrum. Methods **80**, 339 (1970).

[28] C. Goodzeit, R. Meinke, and M. Ball, in Proceedings of the 2007 Particle Accelerator Conference, Albuquerque, New Mexico (Ref. [2]), p. 560 [http://www.JACoW.org].

[29] Vector Fields Software, Brook Road, Wimborne, Dorset, BH21 2BJ, UK.

[30] Bruker Energy & Supercon Technologies, Ehrichstrae 10, 63450 Hanau, Germany.

[31] T. Yokoi, J. Cobb, K. Peach, G. Morgan, J. Pozimski, and M. Easton, in Proceedings of the 11th European Particle Accelerator Conference, Genoa, 2008 (Ref. [9]), p. 3401 [http://www.JACoW.org].

[32] I. S. K. Gardner, in *CERN Accelerator School (92-03),* Vol. II (CERN, Jyväskylä, Finland, 1992), p. 349.

[33] Y. Irie *et al.*, in *Proceedings of EPAC 2011* (JACoW, San Sebastian, Spain, 2011), pp. 2538–2540 [http://www.JACoW.org].

[34] Ferroxcube (UK) Ltd., 2-4 Upper Fairfield Road, Leatherhead, Surrey, KT22 7HH, UK.

[35] Data reproduced from http://www.ferroxcube.com/prod/assets/4e2.pdf [34].

[36] See for example R. Geller, Annu. Rev. Nucl. Sci. **40**, 15 (1990).

[37] M. J. Easton, S. Jolly, J. Pozimski, M. Aslaninejad, and K. Peach, in *Proceedings of the International Particle Accelerator Conference, Kyoto, Japan* (ICR, Kyoto, 2010), p. 822 [http://www.JACoW.org].

[38] B. Schlitt and U. Ratzinger, in *Proceedings of the 6th European Particle Accelerator Conference, Stockholm, 1998* (IOP, London, 1998), p. 2377 [http://www.JACoW.org].

[39] Pulsar Physics, Burghstraat 47, 5614 BC Eindhoven, The Netherlands [http://www.pulsar.nl/gpt].

[40] see for example A. Letchford *et al.*, in Proceedings of the 10th European Particle Accelerator Conference, Edinburgh, Scotland, 2006 (Ref. [21]), pp. 303–305 [http://www.JACoW.org].

[41] Ceramic Magnetics, Inc., 16 Law Drive Fairfield, NJ 07004, USA.

[42] T. Oki, Nucl. Instrum. Methods Phys. Res., Sect. A **607**, 489 (2009).

[43] L. Ducimetiére, in *Proceedings of the 21st Particle Accelerator Conference, Knoxville, 2005* (IEEE, Piscataway, NJ, 2005), p. 235 [http://www.JACoW.org].

[44] General Atomics Electronic Systems, Inc., 4949 Greencraig Lane, San Diego, CA 92123, USA.

[45] TDK (Tokyo Denkikagaku Kogyo) Corporation, 701 Brooks Avenue South, Thief River Falls, MN 56701, USA.

[46] A. Geiger (private communication).

[47] A. Godeke, Ph.D. thesis, University of Twente, Enschede, The Netherlands, 2005.

[48] S. Machida and R. Fenning, Phys. Rev. ST Accel. Beams **13**, 084001 (2010).

[49] J. B. Lagrange and Y. Mori, in *Proceedings of the 23rd Particle Accelerator Conference, Vancouver, Canada, 2009* (IEEE, Piscataway, NJ, 2009), p. 4305.

[50] J. B. Lagrange *et al.*, in *Proceedings of the 3rd International Particle Accelerator Conference, New Orleans, Louisiana, USA, 2012* (IEEE, Piscataway, NJ, 2012).

[51] R. Fenning, in Proceedings of the 23rd Particle Accelerator Conference, Vancouver, Canada, 2009 (Ref. [49]), p. 3741.

[52] U. Weinrich, in Proceedings of the 10th European Particle Accelerator Conference, Edinburgh, Scotland, 2006 (Ref. [21]), p. 964 [http://www.JACoW.org].

[53] E. Fuchs *et al.*, in *Proceedings of EPAC 2004* (JACoW, Tsukuba, Japan, 2004), p. 2550 [http://www.JACoW.org].

[54] D. Trbojević, B. Parker, E. Keil, and A. M. Sessler, Phys. Rev. ST Accel. Beams **10**, 053503 (2007).

[55] R. Fenning, Ph.D. thesis, Brunel University, Uxbridge, UK, 2011; R. Fenning, S. Machida, D. Kelliher, A. Khan, and R. Edgecock, JINST **7**, P05011 (2012).

[56] H. Witte, K. Peach, T. Yokoi, M. Asleninejad, and J. Pasternak, in Proceedings of the 3rd International Particle Accelerator Conference, New Orleans, Louisiana, USA, 2012 (Ref. [50]), pp. 3620–3622.